



Facilely tunable dodecahedral polyoxometalate framework loaded with mono- or bimetallic sites for efficient photocatalytic CO₂ reduction

Bonan Li^{a,1}, Mengxue Chen^{a,1}, Qiyu Hu^a, Jiayu Zhu^a, Xu Yang^a, Zhexu Li^a, Chunlian Hu^a, Yuanyuan Li^d, Ping Ni^e, Yong Ding^{a,b,c,*}

^a State Key Laboratory of Applied Organic Chemistry, Key Laboratory of Advanced Catalysis of Gansu Province, College of Chemistry and Chemical Engineering, Lanzhou University, Lanzhou 730000, China

^b State Key Laboratory of Chemical Resource Engineering, Beijing University of Chemical Technology, Beijing 100029, China

^c State Key Laboratory for Oxo Synthesis and Selective Oxidation, Lanzhou Institute of Chemical Physics, Chinese Academy of Sciences, Lanzhou 730000, China

^d Department of Biological and Chemical Engineering, Chongqing University of Education, Chongqing 400067, China

^e Shandong Zhongke New Material Technology Co., Ltd., Shandong 272503, China

ARTICLE INFO

Keywords:

Polyoxometalates
Morphological evolution
Yolk-shell structure
Non-noble metals
Photocatalytic CO₂ reduction

ABSTRACT

Utilizing solar energy to drive the conversion of CO₂ into high-value chemicals emerged as a promising approach to decrease CO₂ emission. Yolk-shell or hollow structure have drawn much attention for photocatalytic CO₂ reduction, owing to their efficient CO₂ trapping and more active sites exposing. In this study, we employed a simple method to regulate the morphological evolution of K₃PW₁₂O₄₀ dodecahedra. After annealing, mono-/bimetallic active species are homogeneously dispersed on K₃PW₁₂O₄₀ framework forming PW₁₂@Co and PW₁₂@CoNi, which exhibit good CO production rates of 11.2 and 15.1 μmol/h, respectively, with selectivity of 90.7% and 92.6%. The differences in the activity and selectivity of CO₂RR are attributed to the morphology variations of POM and the influence of mono-/bimetallic species. These results are confirmed through the analysis of SEM, TEM, N₂ and CO₂ adsorption/desorption, PL, EIS and SPV characterizations. In-situ DRIFTS and DFT provide further support for the formation and transformation of intermediate products.

1. Introduction

With the rapid development of human civilization and consumption of fossil fuel, excessive CO₂ emissions have led to an annual increase in atmospheric CO₂ concentration [1–3]. The high concentration of CO₂ in the atmosphere has been widely recognized as being related to global environmental problems such as climate change and extreme weather events [4,5]. Therefore, converting the abundant, low-cost and renewable C₁ source carbon dioxide into high value-added chemicals, energy and fuels (e.g., CO, CH₄, HCOOH, etc.) is a green and promising strategy for reducing CO₂ emissions [6,7]. Solar energy is widely recognized as a clean and renewable energy source, making it a crucial element in the transition from fossil fuels to sustainable energy in the future [8]. Inspired by the photosynthesis of biological systems in nature (light reaction: 12 H₂O → 24 H⁺ + 24 e⁻ + 6 O₂; dark reaction: 6 CO₂ + 24 H⁺ + 24 e⁻ → (CH₂O)₆ + 6 H₂O), producing high value-added chemicals with

artificial solar energy has attracted much attention [9]. It is difficult for CO₂ to convert into other carbon-based compounds without harsh reaction conditions since it is a linear molecule with a highly stable, centrally symmetric molecular structure [10]. Hence, regulation the catalyst structure, morphology and the number of active sites could improve the photocatalytic CO₂ reduction reaction (CO₂RR) activity and selectivity [11,12]. In addition, it is desirable to explore low-cost CO₂RR photocatalysts which can mimic the natural photosynthetic systems, while utilizing with abundant elements found on Earth.

In recent years, POMs with well-defined and highly tunable structure and excellent redox property have shown great potential application in the field of photocatalytic CO₂RR [13–15]. Keggin-type H₃PW₁₂O₄₀ is the most typical representative of polyoxometalate, which consists of twelve WO₆ octahedra surrounding a central PO₄ tetrahedron, forming a stable structure with *T_d* symmetry [16–19]. Therefore, H₃PW₁₂O₄₀ possesses the unique ability to maintain its stability even after

* Corresponding author at: State Key Laboratory of Applied Organic Chemistry, Key Laboratory of Advanced Catalysis of Gansu Province, College of Chemistry and Chemical Engineering, Lanzhou University, Lanzhou 730000, China.

E-mail address: dingyong1@lzu.edu.cn (Y. Ding).

¹ These authors contributed equally

undergoing multiple oxidation and reduction reactions. Despite its stability, the $\text{H}_3\text{PW}_{12}\text{O}_{40}$ has limitations for use as a photocatalyst for CO_2RR due to the lack of active sites and its homogeneous catalytic nature in aqueous phase [20–25]. Therefore, few examples for the CO_2RR were reported.

To achieve high activity and selectivity for CO_2RR , photocatalysts should not only possess excellent physicochemical properties and a sufficient number of active sites, but also has the microstructure to be rationally designed. Hollow catalysts are widely considered as the optimal choice for CO_2RR photocatalysis due to their unique microstructural characteristics [26]. Hollow structure catalysis is beneficial for substrate enrichment because of its unique structure [27,28]. Particularly in gas-solid-liquid three-phase catalytic reactions, the large surface area and CO_2 enrichment caused by the hollow structure offer significant advantage for the CO_2 conversion. However, the synthesis of hollow structure with well-defined geometry and controllable etching surface is a challenge [29,30]. To date, the combination of hollow structure and POMs has mostly involved the use of semiconductors and carbon materials as hollow support with surface and cavity enriched POMs as catalytic active sites [14]. However, the use of POMs as hollow structure support with surface loaded active sites for CO_2RR has been rarely reported [31].

In this work, we employed a hydrothermal etching followed by annealing method to transform the heterogeneous $\text{K}_3\text{PW}_{12}\text{O}_{40}$ from its solid dodecahedral structure into a yolk-shell structure, and ultimately it was converted into a hollow structure. Simultaneously, the N_2 thermal decomposition resulted in the in-situ encapsulation of Co or CoNi active sites within the $\text{K}_3\text{PW}_{12}\text{O}_{40}$ framework ($\text{PW}_{12}@\text{Co}$ and $\text{PW}_{12}@\text{CoNi}$), making it a good photocatalyst for CO_2RR . Specifically, $\text{PW}_{12}@\text{Co}$ -6 h and $\text{PW}_{12}@\text{Co-1/6Ni}$ -6 h exhibit CO generation rates of $11.2\ \mu\text{mol/h}$ and $15.1\ \mu\text{mol/h}$ with selectivity of 90.7% and 92.6%, respectively, under photosensitizer system. Noteworthy, besides the variances in CO_2RR activity caused by distinct active sites, the etching effect of the cyanide metal reactant for $\text{K}_3\text{PW}_{12}\text{O}_{40}$ also plays a significant role in influencing both the rate and selectivity of CO_2 reduction. These exceptional performances are attributed to the evolution of the hollow structure within the $\text{K}_3\text{PW}_{12}\text{O}_{40}$ dodecahedra, larger specific surface area, and uniform distribution of surface monometallic/bimetallic sites.

2. Experimental section

2.1. Synthesis of $\text{K}_3\text{PW}_{12}@\text{Co}(\text{CN})_6^{3-}$ ($\text{PW}_{12}@\text{Co}(\text{CN})_6^{3-}$)

$\text{K}_3\text{PW}_{12}@\text{Co}(\text{CN})_6^{3-}$ was synthesized according to a modified literature [32], as follows: 0.332 g of $\text{K}_3\text{Co}(\text{CN})_6$ (1.0 mmol) was dissolved in 20 mL of deionized water to form a homogeneous colorless and transparent solution. Then, 0.30 g of $\text{H}_3\text{PW}_{12}\text{O}_{40}$ dissolved in 6 mL of deionized water was added to the above solution. A white suspension was immediately formed. The white suspension was then transferred to a 50 mL Teflon-lined autoclave and kept at $160\ ^\circ\text{C}$ for various times (3 h, 6 h, 12 h and 24 h). The precipitate was collected by centrifugation, washed three times with water, and dried overnight at $60\ ^\circ\text{C}$. The resulting samples were named: $\text{PW}_{12}@\text{Co}(\text{CN})_6^{3-}$ -0 h, $\text{PW}_{12}@\text{Co}(\text{CN})_6^{3-}$ -3 h, $\text{PW}_{12}@\text{Co}(\text{CN})_6^{3-}$ -6 h, $\text{PW}_{12}@\text{Co}(\text{CN})_6^{3-}$ -12 h and $\text{PW}_{12}@\text{Co}(\text{CN})_6^{3-}$ -24 h.

2.2. Synthesis of $\text{K}_3\text{PW}_{12}@\text{CoNi}(\text{CN})_6^{n-}$ ($\text{PW}_{12}@\text{CoNi}(\text{CN})_6^{n-}$)

The synthesis process of $\text{K}_3\text{PW}_{12}@\text{CoNi}(\text{CN})_6^{n-}$ is the same as that of $\text{K}_3\text{PW}_{12}@\text{Co}(\text{CN})_6^{3-}$, except that $\text{K}_3\text{Co}(\text{CN})_6$ is replaced by a mixture of $\text{K}_3\text{Co}(\text{CN})_6$ and $\text{K}_2\text{Ni}(\text{CN})_4$. The mass of $\text{K}_3\text{Co}(\text{CN})_6$ is 0.332 g (1.0 mmol), and the doping mole ratios of $\text{K}_2\text{Ni}(\text{CN})_4$ are 1/4, 1/6, 1/8 and 1/10 compared to $\text{K}_3\text{Co}(\text{CN})_6$. The yellow suspension was transferred to a 50 mL Teflon-lined autoclave and kept at $160\ ^\circ\text{C}$ for 6 h. The resulting samples were named $\text{PW}_{12}@\text{Co-1/4Ni}(\text{CN})_6^{n-}$, $\text{PW}_{12}@\text{Co-1/6Ni}(\text{CN})_6^{n-}$, $\text{PW}_{12}@\text{Co-1/8Ni}(\text{CN})_6^{n-}$, $\text{PW}_{12}@\text{Co-1/10Ni}(\text{CN})_6^{n-}$.

2.3. Synthesis of $\text{K}_3\text{PW}_{12}@\text{Co}$ ($\text{PW}_{12}@\text{Co}$)

The $\text{PW}_{12}@\text{Co}(\text{CN})_6^{3-}$ was transformed into PW_{12} doped with Co, N, and C by heating the hydrothermally obtained $\text{PW}_{12}@\text{Co}(\text{CN})_6^{3-}$ under N_2 atmosphere at a rate of $1\ ^\circ\text{C}/\text{min}$ to $500\ ^\circ\text{C}$, holding at $500\ ^\circ\text{C}$ for 3 h, and naturally cooling to room temperature. Depending on the hydrothermal time, the resulting products were named $\text{PW}_{12}@\text{Co}$ -0 h, $\text{PW}_{12}@\text{Co}$ -3 h, $\text{PW}_{12}@\text{Co}$ -6 h, $\text{PW}_{12}@\text{Co}$ -12 h and $\text{PW}_{12}@\text{Co}$ -24 h, respectively.

2.4. Synthesis of $\text{K}_3\text{PW}_{12}@\text{CoNi}$ ($\text{PW}_{12}@\text{CoNi}$)

The synthesis process of $\text{K}_3\text{PW}_{12}@\text{CoNi}$ is similar to that of $\text{K}_3\text{PW}_{12}@\text{Co}$, except that the hydrothermally obtained product was replaced with $\text{K}_3\text{PW}_{12}@\text{CoNi}(\text{CN})_6^{n-}$ with different mass ratios of $\text{K}_3\text{Co}(\text{CN})_6$ and $\text{K}_2\text{Ni}(\text{CN})_4$, and named $\text{PW}_{12}@\text{Co-1/4Ni}$, $\text{PW}_{12}@\text{Co-1/6Ni}$, $\text{PW}_{12}@\text{Co-1/8Ni}$ and $\text{PW}_{12}@\text{Co-1/10Ni}$, respectively (the optimally doped ratio of $\text{PW}_{12}@\text{Co-1/6Ni}$ was also named $\text{PW}_{12}@\text{CoNi}$ -6).

2.5. Synthesis of $\text{K}_3\text{PW}_{12}@\text{Cl}^-$ ($\text{PW}_{12}@\text{Cl}^-$)

The synthesis of $\text{K}_3\text{PW}_{12}@\text{Cl}^-$ is similar to that of $\text{K}_3\text{PW}_{12}@\text{Co}(\text{CN})_6^{3-}$, except that $\text{K}_3\text{Co}(\text{CN})_6$ in the latter was replaced with KCl.

2.6. Photocatalytic CO_2 reduction

Photocatalytic CO_2 reduction experiments were conducted in a 69 mL flask irradiated by the same 460 nm LED with the intensity of $100\ \text{mW cm}^{-2}$. The photocatalytic CO_2 reduction reaction was conducted as follows: 15 mg $[\text{Ru}(\text{bpy})_3]\text{Cl}_2$, 12 mL reaction solution [CH_3CN : TEOA : H_2O = 4:1:1 (Vol. ratio)] and 3 mg catalyst were added to the above flask sealed with rubber plug. Before each reaction, CO_2 gas was bubbled into the reaction solution for approximately 10 min. The amount of generated gas was analyzed by gas chromatography (Fuli GC9790Plus) equipped with a thermal conductivity detector (TCD) and a flame ionization detector (FID).

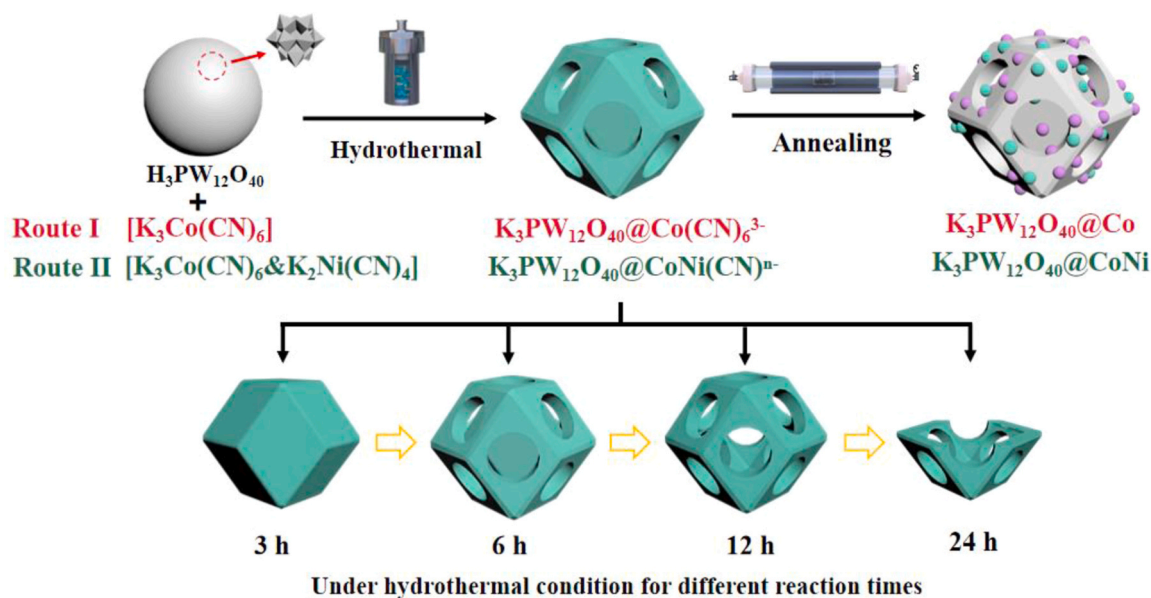
2.7. Electrochemical experiments

Electrochemical tests were performed using an electrochemical workstation (CHI760E) with a 300 W xenon lamp as a light source. A classical three-electrode system was used with 0.5 M Na_2SO_4 solution as electrolyte. The GC electrode/FTO glass, Pt wire and Ag/AgCl (3.0 M KCl, 0.210 V) were used as working, counter and reference electrodes, respectively. 5 mg sample was dispersed in 1 mL ethanol. After 1 h ultrasonic dispersion, a uniform suspension was obtained. Suspension was slowly dropped on the GC electrode/FTO glass and dried under an infrared lamp. Then, 5 μL 0.5 wt% nafion solution was dropped onto the surface of the electrode and dried. The electrode potential is converted to a reversible hydrogen electrode (RHE) by equation $E_{\text{RHE}} = E_{\text{Ag}/\text{AgCl}} + 0.059\ \text{pH} + 0.197$.

3. Result and discussion

3.1. Synthesis and characterization

Through a hydrothermal and annealing process, mono- or bimetallic species (Co or CoNi) are in situ loaded onto the evolved hollow structure $\text{K}_3\text{PW}_{12}\text{O}_{40}$ (Scheme 1). The evolution of the hollow $\text{K}_3\text{PW}_{12}\text{O}_{40}$ loaded with Co monometallic begins with the formation of insoluble $\text{K}_3\text{PW}_{12}\text{O}_{40}$ through ion exchange between a mixture of $\text{H}_3\text{PW}_{12}\text{O}_{40}\cdot n\text{H}_2\text{O}$ and $\text{K}_3[\text{Co}(\text{CN})_6]$. In this process, H^+ reacts with $\text{Co}(\text{CN})_6^{3-}$ to form $\text{H}_3[\text{Co}(\text{CN})_6]$, which is then loaded on the $\text{K}_3\text{PW}_{12}\text{O}_{40}$. The resulting suspension is then subjected to hydrothermal treatment for 3, 6, 12 and 24 h. During this process, the high concentration of H^+ in the system results in a strongly acidic suspension, leading to the uniform



Scheme 1. Schematic illustration of the formation of hydrothermal intermediate product $\text{K}_3\text{PW}_{12}\text{O}_{40}@\text{Co}(\text{CN})_6^{3-}$ / $\text{K}_3\text{PW}_{12}\text{O}_{40}@\text{CoNi}(\text{CN})^n-$ and annealed product $\text{K}_3\text{PW}_{12}\text{O}_{40}@\text{Co}$ / $\text{K}_3\text{PW}_{12}\text{O}_{40}@\text{CoNi}$.

etching of $\text{K}_3\text{PW}_{12}\text{O}_{40}$. As the hydrothermal time increases, the solid dodecahedral structure of $\text{K}_3\text{PW}_{12}\text{O}_{40}$ gradually transforms into a yolk-shell structure, followed by the formation of a hollow structure. When the hydrothermal reaction time prolonged to 24 h, $\text{K}_3\text{PW}_{12}\text{O}_{40}$ dodecahedral structure was collapsed. Subsequently, the hydrothermal intermediate with annealing under N_2 atmosphere causes the $\text{Co}(\text{CN})_6^{3-}$ loaded $\text{K}_3\text{PW}_{12}\text{O}_{40}$ to thermally decompose, forming C, N and mono-metallic Co co-loaded dodecahedral $\text{K}_3\text{PW}_{12}\text{O}_{40}$ structure ($\text{PW}_{12}@\text{Co}$). The C, N and bimetallic CoNi co-loaded dodecahedral $\text{K}_3\text{PW}_{12}\text{O}_{40}$ structure ($\text{PW}_{12}@\text{CoNi}$ -6 h) was synthesized in a similar process to $\text{PW}_{12}@\text{Co}$ -6 h, except that the $\text{K}_3[\text{Co}(\text{CN})_6]$ reactant was replaced with mixtures of different ratios of $\text{K}_3[\text{Co}(\text{CN})_6]$ and $\text{K}_2[\text{Ni}(\text{CN})_4]$.

In order to understand the evolutionary mechanism of $\text{K}_3\text{PW}_{12}\text{O}_{40}$ morphology, the structural evolution of monometallic Co-loaded $\text{PW}_{12}@\text{Co}$ at different hydrothermal times was analyzed by scanning electron microscopy (SEM) (Fig. 1a-d). When the hydrothermal reaction time is

3 h, $\text{PW}_{12}@\text{Co}$ -3 h exhibits a typical solid dodecahedral structure, which appears uniform dodecahedra (Fig. 1a). When the hydrothermal time is extended to 6 h, the dodecahedral structure of $\text{PW}_{12}@\text{Co}$ -6 h undergoes partially uniform etching, resulting in the formation of a yolk-shell structure with a size around 1.5 μm (Fig. 1b). This structural transformation is attributed to the acidity of the solution system. When the hydrothermal time is prolonged to 12 h, the dodecahedral structure of $\text{PW}_{12}@\text{Co}$ -12 h undergoes further internal etching, and all twelve faces undergo uniformly complete etching, resulting in the formation of a hollow dodecahedra with a size of around 1.75 μm (Fig. 1c). Further extension of the hydrothermal time to 24 h results in the collapse of the hollow structure (Fig. 1d). When KCl is used as a substitute for $\text{K}_3[\text{Co}(\text{CN})_6]$ in the synthesis of $\text{K}_3\text{PW}_{12}\text{O}_{40}$, an etching effect can also be observed (Fig. S1). This is because the Cl^- in the system can bind with H^+ to form HCl, and the acidity of HCl is stronger than that of $\text{H}_3[\text{Co}(\text{CN})_6]$. As a result, at a hydrothermal duration of 2 h, $\text{PW}_{12}@\text{Cl}^-$ exhibits a yolk-

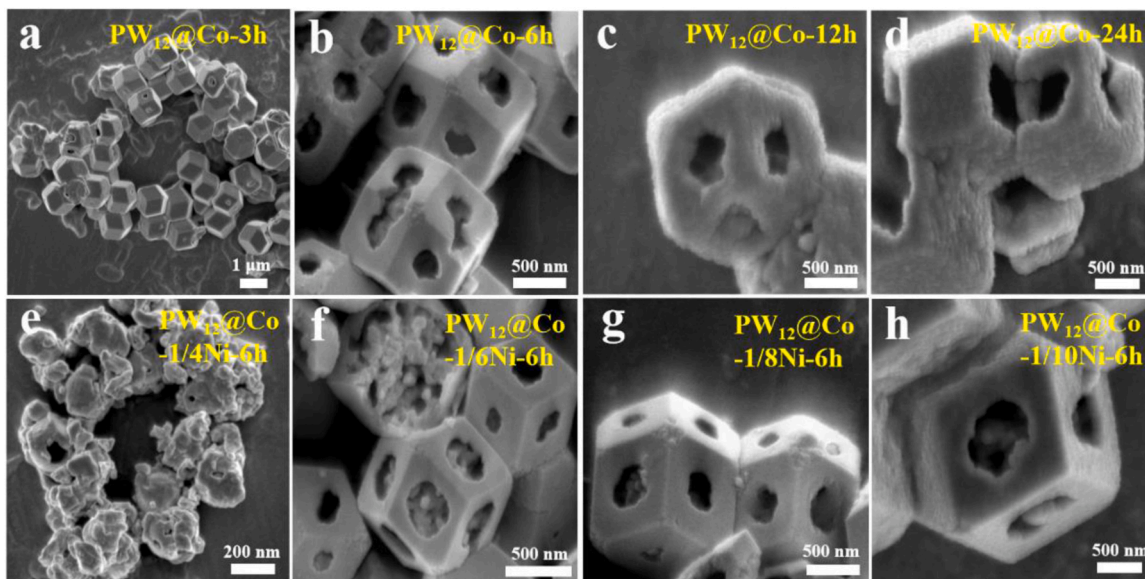


Fig. 1. SEM images of (a) $\text{PW}_{12}@\text{Co}$ -3 h, (b) $\text{PW}_{12}@\text{Co}$ -6 h, (c) $\text{PW}_{12}@\text{Co}$ -12 h, (d) $\text{PW}_{12}@\text{Co}$ -24 h, (e) $\text{PW}_{12}@\text{Co}$ -1/4Ni-6 h, (f) $\text{PW}_{12}@\text{Co}$ -1/6Ni-6 h, (g-h) $\text{PW}_{12}@\text{Co}$ -1/8Ni-6 h and $\text{PW}_{12}@\text{Co}$ -1/10Ni-6 h.

shell structure similar to $\text{PW}_{12}@Co-6\text{ h}$.

To investigate the effect of different Co/Ni loading ratios on the structure of $\text{K}_3\text{PW}_{12}\text{O}_{40}$ dodecahedra, the morphology of bimetallic $\text{PW}_{12}@CoNi$ was characterized using SEM. Since the synthesis of $\text{PW}_{12}@Co$ with a yolk-shell structure was conducted under the conditions of maintaining 1 mmol $\text{K}_3\text{Co}(\text{CN})_6$ and a 6 h hydrothermal time. For $\text{PW}_{12}@CoNi$, on the same foundation, different proportions of $\text{K}_2\text{Ni}(\text{CN})_4$ are introduced. When the proportion of Ni introduced exceeds 1/6, $\text{K}_3\text{PW}_{12}\text{O}_{40}$ in the composite catalyst almost disappears (Fig. 1e and S3), suggesting a chemical interaction between the introduced $\text{K}_2\text{Ni}(\text{CN})_4$ and $\text{K}_3\text{PW}_{12}\text{O}_{40}$ during the hydrothermal process. When the proportion of Ni introduced is less than or equal to 1/6, $\text{K}_3\text{PW}_{12}\text{O}_{40}$ is significantly in excess compared to $\text{K}_2\text{Ni}(\text{CN})_4$, resulting in only non-uniform etching while maintaining the intact yolk-shell structure (Fig. 1f-h and Fig. 2a-b). In conclusion, a loading ratio of the second metal Ni equal to or less than 1/6 maintains the yolk-shell structure of $\text{K}_3\text{PW}_{12}\text{O}_{40}$ well, causing only non-uniform etching.

The transmission electron microscopy (TEM) images of $\text{PW}_{12}@Co-6\text{ h}$ and $\text{PW}_{12}@Co-1/6Ni-6\text{ h}$ provide a comprehensive understanding of their complicated internal yolk-shell spatial configurations. Meanwhile, TEMs reveal the etching extent after undergoing mono- and bimetallic loading processes. Fig. 2a indicate a uniform etching throughout $\text{PW}_{12}@Co-6\text{ h}$, while Fig. 2b reveal that the internal etching of the dodecahedral structure of $\text{PW}_{12}@Co-1/6Ni-6\text{ h}$ is not uniform. Nevertheless, the dodecahedral framework of PW_{12} remains well-maintained despite the non-uniform etching. The asymmetric etching of $\text{PW}_{12}@Co-1/6Ni-6\text{ h}$ serves to enhance its specific surface area, which subsequently exposes a larger number of metallic sites. Furthermore, the elemental mapping of $\text{PW}_{12}@Co-6\text{ h}$ and $\text{PW}_{12}@Co-1/6Ni-6\text{ h}$ illustrates a well-distributed array of elements, with $\text{PW}_{12}@Co-6\text{ h}$ containing Co, O, P and W, and $\text{PW}_{12}@Co-1/6Ni-6\text{ h}$ containing Co, Ni, O, P and W (Fig. 2c-f). Meanwhile, the HRTEM image of $\text{PW}_{12}@Co-1/6Ni-6\text{ h}$ reveals that Co/Ni metal sites are uniformly loaded on the dodecahedral structure, with a lattice spacing of 0.206 nm, which corresponds to the (111) crystal plane of element Co or Ni (Fig. 2g-h).

To confirm the yolk-shell dodecahedral structure of $\text{K}_3\text{PW}_{12}\text{O}_{40}$ after hydrothermal annealing process, infrared spectroscopy (IR) and powder X-ray diffraction (PXRD) were performed. In the IR spectra, the hydrothermal intermediates $\text{PW}_{12}@Co(\text{CN})_6^{3-}$ and $\text{PW}_{12}@CoNi(\text{CN})_6^{4-}$ exhibit characteristic peaks at 803.2, 891.8, 988.3 and 1080.1 cm^{-1} , which correspond to the W-O-W, W=O, and P-O-W vibration of $\text{K}_3\text{PW}_{12}\text{O}_{40}$, respectively (Fig. S2) [33]. Furthermore, the $\text{N}\equiv\text{C}$ vibrational peak

observed at approximately $\sim 2180\text{ cm}^{-1}$ can be attributed to the $\text{Co}(\text{CN})_6^{3-}$ and $\text{Ni}(\text{CN})_4^{2-}$ species loaded on the $\text{K}_3\text{PW}_{12}\text{O}_{40}$ framework. The characteristic peaks of $\text{K}_3\text{PW}_{12}\text{O}_{40}$ are observed in the range of 800–1100 cm^{-1} after annealing for both $\text{PW}_{12}@Co$ and $\text{PW}_{12}@CoNi$, indicating the preservation of the framework structure of $\text{K}_3\text{PW}_{12}\text{O}_{40}$. Additionally, the $\text{N}\equiv\text{C}$ characteristic vibration peak at 2180 cm^{-1} disappears after annealing, indicating that $\text{Co}(\text{CN})_6^{3-}$ and $\text{Ni}(\text{CN})_4^{2-}$ are convert to Co/CoNi, C and N, which are loaded in the $\text{K}_3\text{PW}_{12}\text{O}_{40}$ framework during annealing (Fig. 3a-b). In particular, when the Ni/Co doping ratio in $\text{PW}_{12}@CoNi$ is higher than 1/6, the characteristic vibration peak of $\text{K}_3\text{PW}_{12}\text{O}_{40}$ at 800–1000 cm^{-1} nearly disappear, which can be attributed to the $\text{Ni}(\text{CN})_4^{2-}$ during ion exchange in the hydrothermal process (Fig. S3). This is consistent with the results of SEM and TEM image analysis of $\text{PW}_{12}@Co$ and $\text{PW}_{12}@CoNi$.

Additionally, powder X-ray diffractometer (PXRD) was employed to analyze the crystallinity and composition of the samples. Consistent characteristic diffraction peaks are observed in $\text{PW}_{12}@Cl^-$, hydrothermal intermediate $\text{PW}_{12}@Co(\text{CN})_6^{3-}$, as well as annealed samples $\text{PW}_{12}@Co-6\text{ h}$ and $\text{PW}_{12}@Co-12\text{ h}$. These diffraction peaks are almost the same as that of the standard card PDF#70-0129 which represents Keggin-type $\text{K}_3\text{PW}_{12}\text{O}_{40}$ (Fig. 3c). Samples $\text{PW}_{12}@Co-1/6Ni$, $\text{PW}_{12}@Co-1/8Ni$ and $\text{PW}_{12}@Co-1/10Ni$ with different Co/Ni loading ratios have remarkable consistency with Keggin-type $\text{K}_3\text{PW}_{12}\text{O}_{40}$. However, when the Co/Ni loading ratio is 1/4, $\text{PW}_{12}@Co-1/4Ni$ is different with the standard card of $\text{K}_3\text{PW}_{12}\text{O}_{40}$. (Fig. 3d). According to the comprehensive XRD analysis results, it can be further demonstrated that samples $\text{PW}_{12}@Co$ and $\text{PW}_{12}@CoNi$ with dodecahedral structures are well-preserved after hydrothermal and annealing.

Moreover, when Co/Ni was loaded on $\text{K}_3\text{PW}_{12}\text{O}_{40}$, the strongest diffraction peaks of $\text{PW}_{12}@Co-6\text{ h}$ and $\text{PW}_{12}@Co-1/6Ni-6\text{ h}$ appear a slight shift in the diffraction angle at $26.5\text{--}27.0^\circ$ compared with the XRD pattern of $\text{PW}_{12}@Cl^-$ (Fig. S4). Additionally, the XRD analysis confirms that excessive $\text{Ni}(\text{CN})_4^{2-}$ completely corrodes the $\text{K}_3\text{PW}_{12}\text{O}_{40}$ during the hydrothermal ion exchange process. The results of the ICP test show that the ratio of Co and W in the $\text{PW}_{12}@Co-6\text{ h}$ sample is 1:5.66. In the $\text{PW}_{12}@Co-1/6Ni$ sample, the ratio of Co, Ni and W is 1:1:10.5 (Table S1). Due to the relatively low content of Co and Ni, characteristic peaks of Co or Ni in the samples are not observed in the XRD patterns of $\text{PW}_{12}@Co-6\text{ h}$ and $\text{PW}_{12}@Co-1/6Ni$. Elemental analysis of organic components demonstrated an increase in C and N contents in $\text{PW}_{12}@Co$ with prolonged hydrothermal treatment time. This indicates that the yolk-shell structure effectively enriches the metallic sites along with C and N.

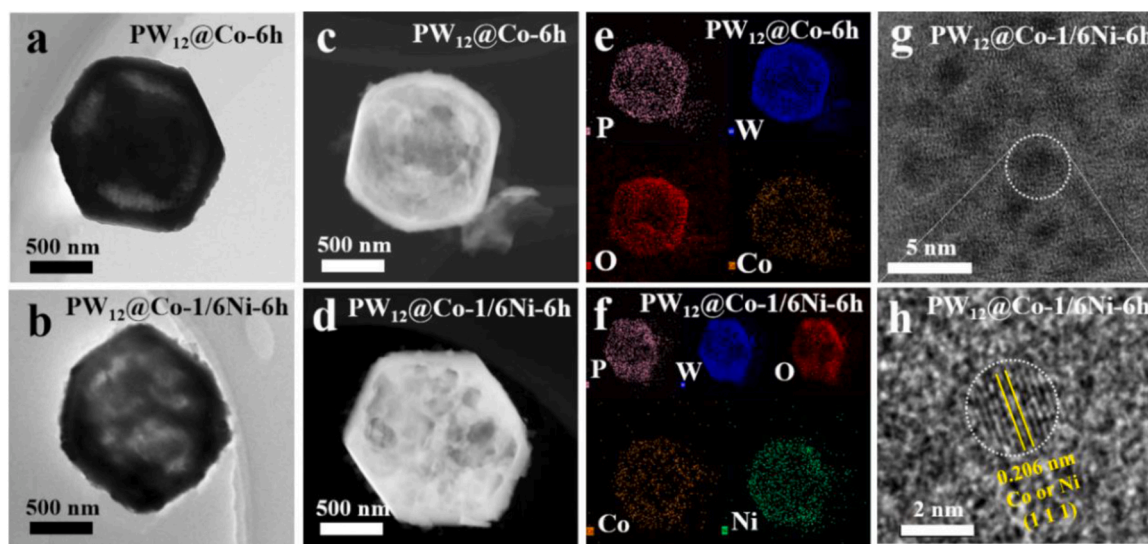


Fig. 2. TEM image of (a) $\text{PW}_{12}@Co-6\text{ h}$, (b) $\text{PW}_{12}@Co-1/6Ni-6\text{ h}$, HAADF-STEM of (c) $\text{PW}_{12}@Co-6\text{ h}$ and (d) $\text{PW}_{12}@Co-1/6Ni-6\text{ h}$, EDX mapping of the various elements contained of (e) $\text{PW}_{12}@Co-6\text{ h}$ and (f) $\text{PW}_{12}@Co-1/6Ni-6\text{ h}$, (g-h) HRTEM image of $\text{PW}_{12}@Co-1/6Ni-6\text{ h}$ from magnified white circle.

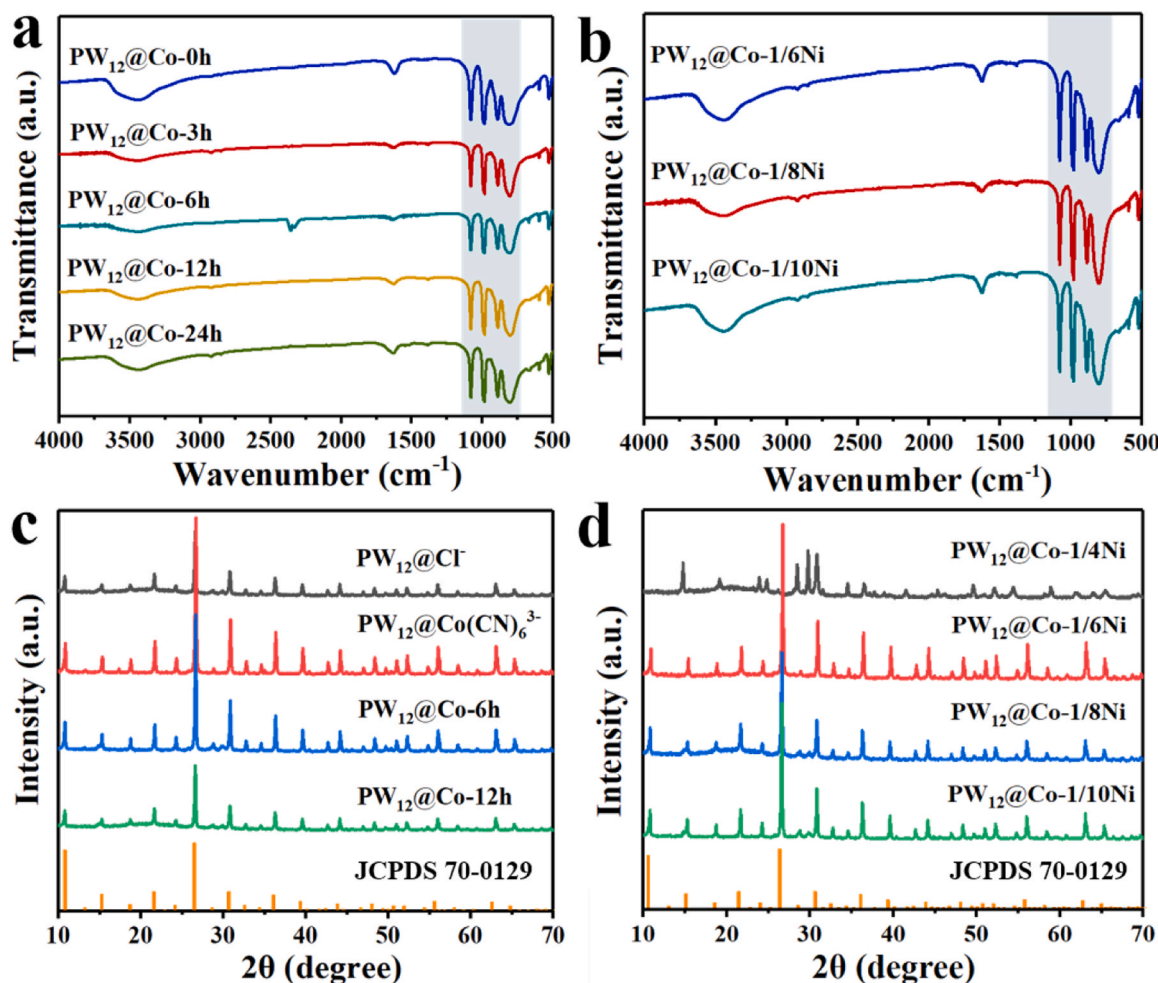


Fig. 3. IR spectra of (a) $\text{PW}_{12}@\text{Co}$ with different hydrothermal reaction times, (b) $\text{PW}_{12}@\text{CoNi}$ -6 h different Co/Ni loading ratios, XRD patterns of (c) $\text{PW}_{12}@\text{Cl}^-$, $\text{PW}_{12}@\text{Co}(\text{CN})_6^{3-}$, $\text{PW}_{12}@\text{Co}$ and (d) $\text{PW}_{12}@\text{CoNi}$ -6 h with different Co/Ni loading ratios.

Furthermore, $\text{PW}_{12}@\text{Co-1/6Ni}$ -6 h exhibited higher contents of C and N compared to $\text{PW}_{12}@\text{Co-6 h}$, suggesting that the unevenly etched yolk-shell structure of $\text{PW}_{12}@\text{Co-1/6Ni}$ -6 h has a greater capacity for enriching metallic sites as well as C and N elements (Table S2).

The optical properties of the aforementioned photocatalysts are investigated using UV-vis diffuse reflectance spectroscopy (DRS, Fig. S5). $\text{PW}_{12}@\text{Cl}^-$ shows strong absorption only in the UV region, while $\text{PW}_{12}@\text{Co}(\text{CN})_6^{3-}$ and $\text{PW}_{12}@\text{CoNi}(\text{CN})_6^{3-}$ -6 h both exhibit partial visible light absorption in a range 400–550 nm after undergoing ion exchange and hydrothermal processes. This phenomenon indicates that $\text{Co}(\text{CN})_6^{3-}$ and $\text{Ni}(\text{CN})_4^{2-}$ are successfully encapsulated within the $\text{K}_3\text{PW}_{12}\text{O}_{40}$ framework. After annealing, $\text{PW}_{12}@\text{Co-6 h}$ and $\text{PW}_{12}@\text{Co-1/6Ni}$ -6 display broad and strong absorption in the visible light region. The band energy levels of photosensitizer (PS), $\text{PW}_{12}@\text{Co-6 h}$ and $\text{PW}_{12}@\text{Co-1/6Ni}$, as deduced from combination DRS, Tauc-plot and Mott-Schottky tests, obey the thermodynamic prerequisites essential for accomplishing photocatalytic CO_2 conversion (Fig. S6–S7). In essence, these materials demonstrate the ability required for the reduction potential of CO_2 to CO (Fig. S8).

X-ray photoelectron spectroscopy (XPS) was used to characterize the surface chemical composition and valence states of $\text{PW}_{12}@\text{Co-6 h}$ and $\text{PW}_{12}@\text{Co-1/6Ni}$. Due to the similar surface chemical composition and valence states of $\text{PW}_{12}@\text{Co-6 h}$ and $\text{PW}_{12}@\text{Co-1/6Ni}$, $\text{PW}_{12}@\text{Co-1/6Ni}$ is used as an example for analysis. The XPS survey spectrum of $\text{PW}_{12}@\text{CoNi}$ reveals the presence of Co, Ni, C, N, P, W, and O (Fig. S9), which is consistent with the elemental mapping analysis. Specifically, the K 2p

peaks for $\text{K}_3\text{PW}_{12}\text{O}_{40}$ are located at 292.7 and 295.5 eV, the P 2p peak at 133.5 eV, the W 4f peaks at 35.5 and 37.6 eV, and the O 1s peaks at 530.1 and 531.4 eV [34]. In addition, for the Co and Ni loaded on the $\text{K}_3\text{PW}_{12}\text{O}_{40}$ framework, the peaks located at 778.7 ($2p_{3/2}$) and 793.6 eV ($2p_{1/2}$) can be ascribed to the Co^0 . The peaks located at 780.0/795.6 eV and 782.2/797.9 eV are associated with the Co^{3+} and Co^{2+} oxidation states, accompanied by their satellite peaks at 786.5 eV and 802.4 eV [35,36]. The peaks at 852.9 ($2p_{3/2}$) and 870.4 eV ($2p_{1/2}$) can be ascribed to the Ni^0 . The peaks at 853.9/871.5 eV and 855.8/874.0 eV are associated with the Ni^{2+} and Ni^{3+} oxidation states, accompanied by their satellite peaks at 860.2 eV and 877.9 eV (Fig. 4) [37]. Furthermore, the high-resolution spectrum of C1s for $\text{PW}_{12}@\text{Co-1/6Ni}$ could be deconvoluted into three carbon species assigned to the C-C (284.1 eV), C=N (286.4.0 eV) and graphitic carbon (289.0 eV), respectively. The presence of C=N species verified the successful introduction of nitrogen in graphitic carbon (Fig. S10) [38]. Raman spectroscopy of $\text{PW}_{12}@\text{Co-1/6Ni}$ -6 h reveals characteristic peaks of graphitic carbon D and G bands at 1350 cm^{-1} and 1580 cm^{-1} (Fig. S11) [39]. The high-resolution N 1s spectrum of the hydrothermal intermediate $\text{PW}_{12}@\text{CoNi}(\text{CN})_6^{3-}$ exhibits a characteristic peak at 398.4 eV, which is attributed to $\text{N}\equiv\text{C}$ on the $\text{K}_3\text{PW}_{12}\text{O}_{40}$ framework loaded with $\text{Co}(\text{CN})_6^{3-}$ and $\text{Ni}(\text{CN})_4^{2-}$ [9]. After annealing, binding energy of N 1s in $\text{PW}_{12}@\text{Co-1/6Ni}$ changes to 397.7, 399.4.0 and 401.30 eV, which is assigned to the pyridinic N, pyrrolic N and graphitic N (Fig. S12) [40]. Therefore, the form of C and N elements is as N-doped graphitic carbon.

The aforementioned XPS analysis confirms the coexistence of Co^0

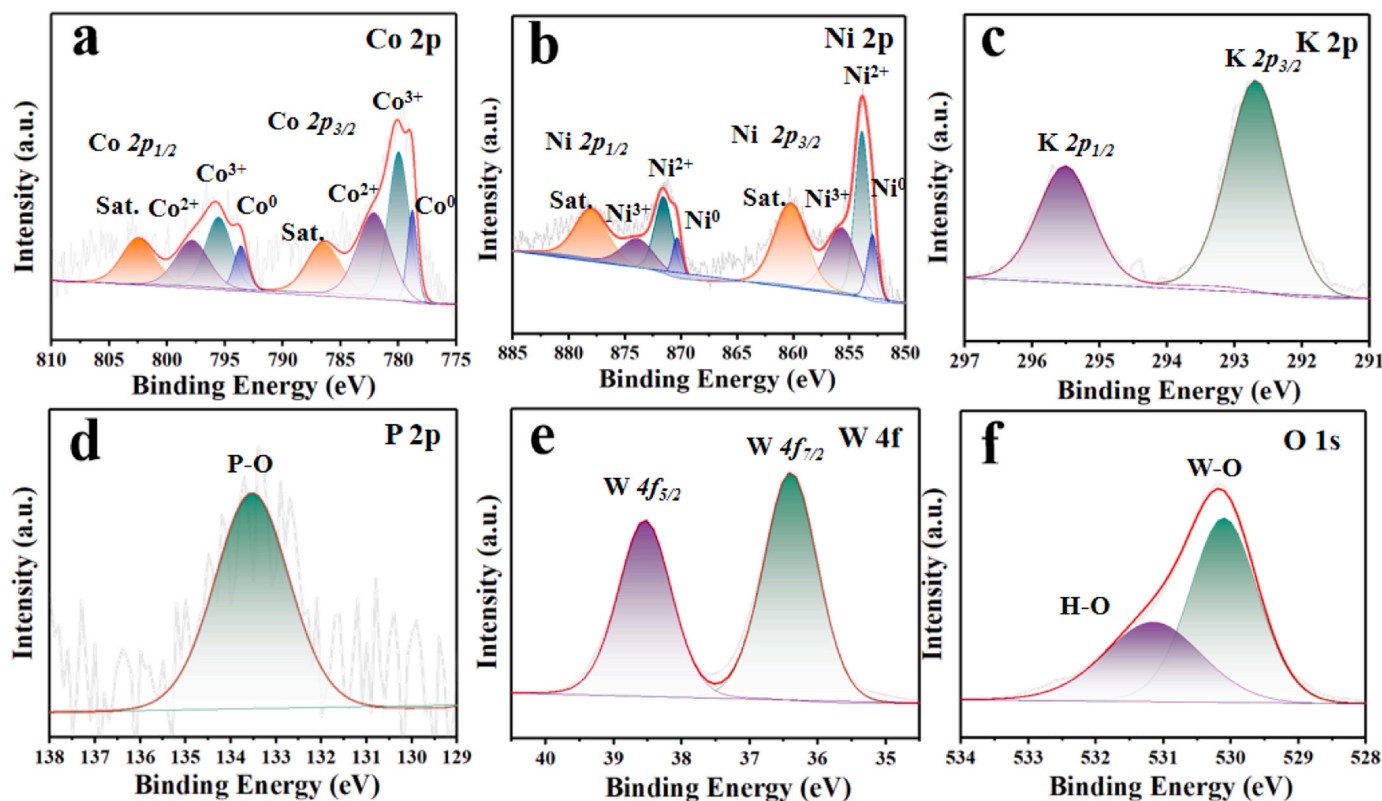


Fig. 4. High resolution XPS spectra of (a) Co 2p, (b) Ni 2p, (c) K 2p, (d) P 2p, (e) W 4f and (f) O 1s for $\text{PW}_{12} @\text{Co-1/6Ni-6 h}$.

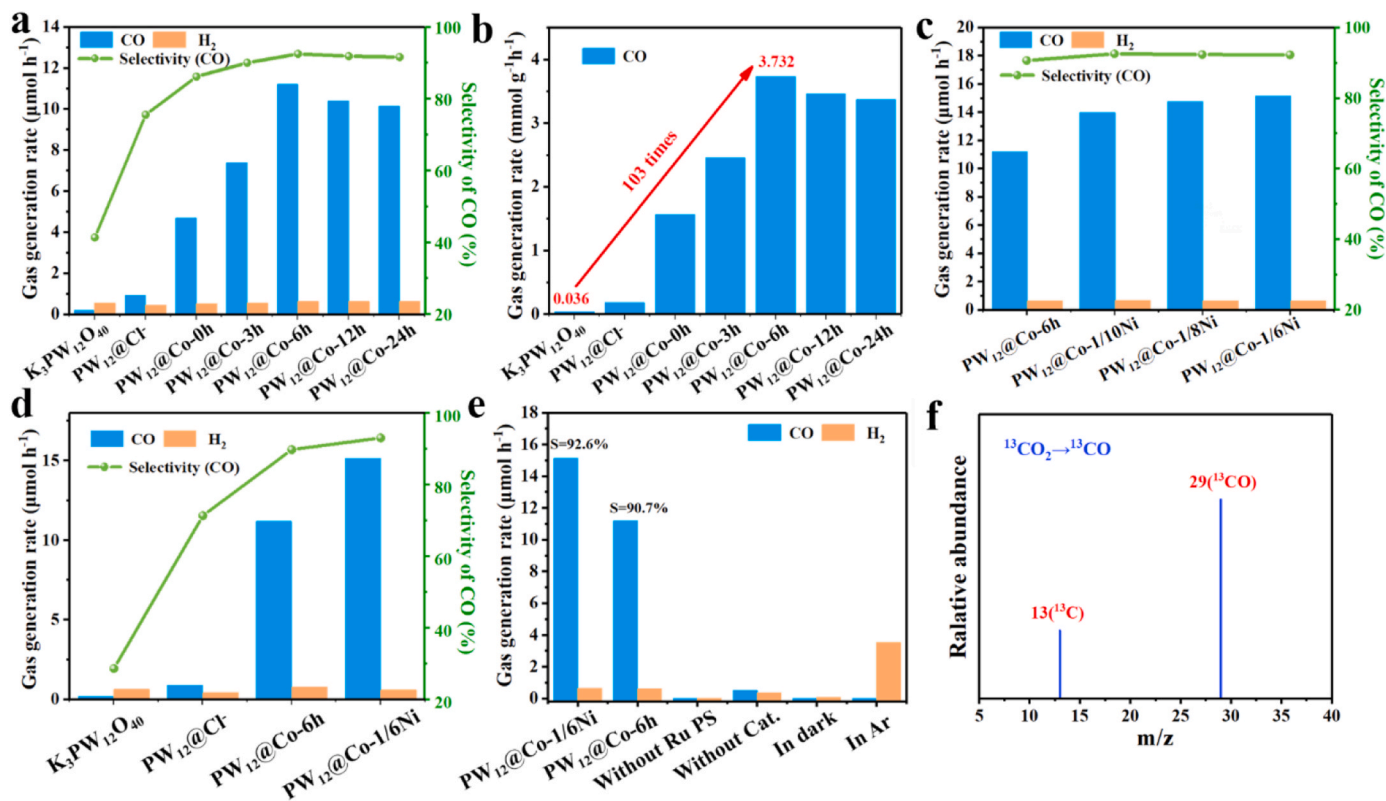


Fig. 5. (a-b) Comparison of CO_2RR activity and selectivity of $\text{K}_3\text{PW}_{12}\text{O}_{40}$, $\text{PW}_{12} @\text{Cl}^-$ and $\text{PW}_{12} @\text{Co}$ with different hydrothermal reaction times, (c) Comparison of CO_2RR activity and selectivity of $\text{PW}_{12} @\text{CoNi}$ with different Co/Ni loading ratios, (d) Comparison of CO_2RR activity and selectivity of main photocatalysts, (e) Single variable experiments for the CO_2RR and (f) ^{13}C isotope marker experiment of $\text{PW}_{12} @\text{Co-1/6Ni-6 h}$.

and Ni⁰ species with their respective oxide states, which may be attributed to surface oxidation. The survey and high-resolution spectra of various elements obtained from XPS further confirm the successful loading of Co, Ni, C, and N elements within the yolk-shell K₃PW₁₂O₄₀ structure. In order to deeply investigate the electron transfer direction in PW₁₂@Co-6 h and PW₁₂@Co-1/6Ni, a supplementary test on the W 4f fine spectrum of K₃PW₁₂O₄₀ was conducted. When Co or CoNi is loaded on the K₃PW₁₂O₄₀, the binding energy values of the W 4f in PW₁₂@Co-6 h and PW₁₂@Co-1/6Ni shift positively, confirming that the Co or CoNi have been successfully loaded on K₃PW₁₂O₄₀ and that there is a strong interaction between them (Fig. S15).

3.2. Photocatalytic CO₂ reduction activity evaluation

The photocatalytic CO₂ reduction reaction was carried out in a mixed solution of MeCN/H₂O (4:1) in a pure CO₂ atmosphere (25 °C, 1.0 atm) with TEOA as the sacrificial agent and [Ru(bpy)₃]Cl₂·6 H₂O as the photosensitizer. The maximum absorption wavelength of [Ru(bpy)₃]²⁺ is 455 nm. Therefore, a 460 nm LED light was used for the photocatalytic CO₂ reduction performance evaluation, ensuring that [Ru(bpy)₃]²⁺ can be fully excited (Fig. S16).

Both K₃PW₁₂O₄₀ and unmodified yolk-shell structure PW₁₂@Cl⁻ exhibit low activity in photocatalytic CO₂ reduction, with the H₂ yield of K₃PW₁₂O₄₀ even higher than that of CO. The structure of yolk-shell PW₁₂@Cl⁻ exhibit a physical adsorption effect on CO₂. Although the CO₂ reduction activity is relatively low, the CO selectivity is higher than that of H₂ (Fig. 5a). Notably, all monometallic-loaded PW₁₂@Co samples show a significant increase in CO₂ reduction activity. Hence, the impact of different structures resulting from varying hydrothermal treatment times on the CO₂ reduction activity and selectivity is investigated over PW₁₂@Co. Due to its lack of hydrothermal etching, PW₁₂@Co-0 h exhibits only a moderate improvement with a CO generation rate of 4.7 μmol/h and a selectivity of 82.8%. As the hydrothermal time increases to 3 h, PW₁₂@Co-3 h with a solid dodecahedral structure shows improved activity and selectivity compared to PW₁₂@Co-0 h. Specifically, it exhibits a CO generation rate of 7.4 μmol/h and a selectivity of 87.6%. The PW₁₂@Co-6 h with a yolk-shell dodecahedral structure obtained at a hydrothermal time of 6 h exhibits the highest CO production rate of 11.2 μmol/h and a selectivity of 90.7%.

When the hydrothermal time is 12 h, the dodecahedral structure of K₃PW₁₂O₄₀ is etched into a hollow structure. PW₁₂@Co-12 h possesses a pore size of approximately 450 nm, which is much larger than the size of CO₂ (0.35 nm). Hence, the hollow structure of PW₁₂@Co-12 h cannot effectively adsorb CO₂. Therefore, its photocatalytic activity and selectivity for CO₂ reduction are lower than that of PW₁₂@Co-6 h, with CO generation rate of 10.4 μmol/h and selectivity of 89.9% respectively. When the hydrothermal time is extended to 24 h, PW₁₂@Co-24 h with a collapsed K₃PW₁₂O₄₀ framework structure exhibits lower activity and selectivity compared with PW₁₂@Co-12 h. Furthermore, the CO mass evolution rate of PW₁₂@Co-6 h (3.7 mmol/g/h) is 103 times higher than that of commercial K₃PW₁₂O₄₀ (0.04 mmol/g/h) (Fig. 5b). Based on the analysis of the aforementioned activity and selectivity, it can be concluded that the addition of Co active sites onto the K₃PW₁₂O₄₀ framework through hydrothermal and annealing effectively enhance the activity and selectivity for photocatalytic CO₂ reduction.

When Co and Ni are loaded onto the K₃PW₁₂O₄₀ framework, they offer more active sites compared to monometallic loading, and the uneven etching process inside the structure results in a larger specific surface area (Table S3) and enhanced CO₂ adsorption. Consequently, PW₁₂@CoNi exhibits better photocatalytic CO₂ reduction rate and selectivity compared to PW₁₂@Co. Specifically, when different ratios of Co and Ni (10:1, 8:1, 6:1) are loaded on the K₃PW₁₂O₄₀ framework, they all display higher CO₂ reduction rate and selectivity, with values of 14.0, 14.7, 15.1 μmol/h and 92.3%, 92.4%, 92.6%, respectively (Fig. 5c). By comparing the CO evolution over several photocatalysts, it is found that the yolk-shell structures PW₁₂@Co-6 h and PW₁₂@CoNi-6 h exhibit

significantly improved CO₂ reduction rate and selectivity compared to commercialized K₃PW₁₂O₄₀ and PW₁₂@Cl⁻ (Fig. 5d).

According to the XPS and Raman spectra of C and N for PW₁₂@Co-1/6Ni-6 h, C and N species existed as N-doped graphitic carbon for PW₁₂@Co and PW₁₂@CoNi. In order to investigate the role of C and N species in photocatalytic reactions, we synthesized N-doped graphitic carbon and physically combined it with yolk-shell structured PW₁₂@Cl⁻ to form PW₁₂/CN. In the same photocatalytic CO₂ reduction system, PW₁₂/CN shows poor CO production activity with production rate of 1.18 μmol/h and a selectivity of 69.8% (Fig. S13). Compared PW₁₂@Cl⁻ with the yolk-shell structure, the activity of PW₁₂/CN increases little. Therefore, C and N species should act as byproducts of Co(CN)₆³⁻ and Ni(CN)₄²⁻ during the annealing process. In fact, the true active sites in the catalytic reaction are the annealed Co and Ni species, which significantly improve the photocatalytic CO₂ reduction activity and selectivity.

Through single variable control experiments on photocatalytic CO₂ reduction, it is demonstrated that the catalyst, light source, water, acetonitrile, CO₂ and [Ru(bpy)₃]²⁺ are all necessary conditions for efficient photocatalytic CO₂ reduction (Fig. 5e). Specifically, when the system atmosphere is replaced with Ar, no CO is detected after CO₂RR and only a large amount of H₂ produces. This phenomenon indicates that the CO is generated from the reduction of CO₂ instead of the decomposition of PW₁₂@Co and PW₁₂@CoNi or TEOA. Furthermore, this conclusion is confirmed by ¹³C isotope labeling experiments (Fig. 5f and S17). It is found that the catalyst mass has a significant impact on the CO evolution activity (Fig. S18). The above activity data (rate, mass rate, and selectivity for CO) for PW₁₂@Co-6 h and PW₁₂@Co-1/6Ni are relatively high among the reported photosensitizer-POM photocatalytic CO₂ reduction system (Table S4).

In the photocatalytic CO₂ reduction kinetic curves of PW₁₂@Co-6 h and PW₁₂@Co-1/6Ni-6 h, the production rates of CO and H₂ steadily increase within 150 min (Fig. 6a-b). However, the rate and CO selectivity exhibit a slight decline. This could be attributed to the alkaline of the photocatalytic system in the presence of TEOA, causing the [Ru(bpy)₃]²⁺ to become unstable (Fig. S16). Photocatalytic stability is an important indicator of good photocatalysts. The cyclic stability test shows nearly no decrease in the rate for CO over five cycles, indicating that PW₁₂@Co-6 h and PW₁₂@Co-1/6Ni-6 h have very good stability (Fig. 6c-d).

In order to further evaluate the stability of PW₁₂@Co-6 h and PW₁₂@Co-1/6Ni-6 h, XRD, IR, SEM and XPS measurements are performed on PW₁₂@Co and PW₁₂@CoNi after the photocatalytic CO₂ reduction. After the photocatalytic reaction, the characteristic peak positions of PW₁₂ in IR (Fig. S19) and XRD (Fig. S20) remain unchanged for both catalysts. These results strongly suggest that the yolk-shell structural frameworks of PW₁₂@Co-6 h and PW₁₂@Co-1/6Ni-6 h are quite stable. Furthermore, compared to the SEM image of PW₁₂@Co-1/6Ni before the reaction, the yolk-shell structure of PW₁₂@Co-1/6Ni is maintained after CO₂RR (Fig. S21). Nearly no changes could be observed in the high-resolution XPS spectra of Co 2p and Ni 2p of PW₁₂@Co-1/6Ni before and after photocatalytic CO₂RR (Fig. S22), indicating that the active sites of CoNi metals are well maintained during photocatalytic CO₂RR.

3.3. Photoelectrochemical measurement

The migration rate of photogenerated electrons is a crucial factor that affects the photocatalytic CO₂ reduction. The migration rate is confirmed by steady-state photoluminescence spectra (PL) and electrochemical impedance spectroscopy (EIS). In this study, PW₁₂@Cl⁻, PW₁₂@Co-6 h (PW₁₂@Co) and PW₁₂@Co-1/6Ni-6 h (PW₁₂@CoNi) are selected as examples to explore the difference migration rate of photogenerated electrons in CO₂RR [38,39]. In the photosensitizer photocatalytic CO₂ reduction system, [Ru(bpy)₃]²⁺ is excited by light at a wavelength of 460 nm to generate [Ru(bpy)₃]^{2+*}, which then returns to the ground state through fluorescence quenching. Thus, the fluorescence intensity observed in the PL spectra typically signifies the

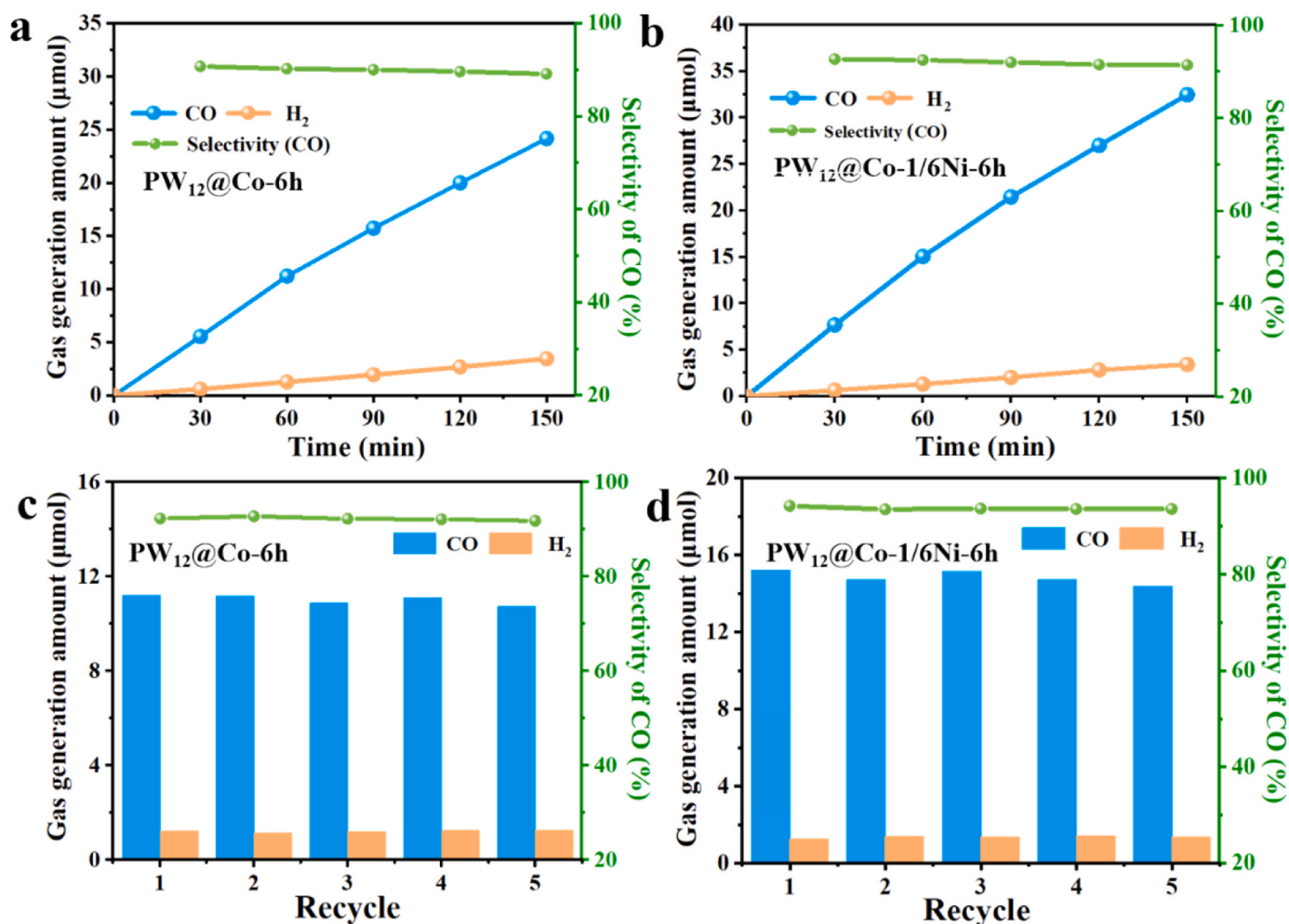


Fig. 6. (a, b) Kinetic curves of photocatalytic CO₂RR tests over 3 mg of PW₁₂@Co-6 h and PW₁₂@Co-1/6Ni-6 h, and (c, d) The recycle experiments of PW₁₂@Co-6 h and PW₁₂@Co-1/6Ni-6 h.

migration efficiency of photogenerated electrons in the photosensitizer. In the pure PS system, the excited state $[\text{Ru}(\text{bpy})_3]^{2+*}$ does not go through the intermediate state $\text{Ru}(\text{bpy})_3^+$, but quickly returns to the ground state through fluorescence quenching, resulting in a high fluorescence intensity. When PW₁₂@Cl⁻, PW₁₂@Co and PW₁₂@CoNi were introduced into the system, the fluorescence intensity decreases, indicating electron transfer takes place between the catalyst and PS as well as improving the migration efficiency of photogenerated electrons (Fig. 7a). PW₁₂@Co and PW₁₂@CoNi have smaller electrochemical impedance compared to PW₁₂@Cl⁻. The PW₁₂@CoNi exhibits the smallest electrochemical impedance value among all samples, indicating that PW₁₂@CoNi has the fastest electron transfer rate between the catalyst and PS (Fig. 7b) [41,42].

3.4. Surface photovoltage spectroscopy investigation

To verify the above characterization results, surface photovoltage spectroscopy (SPV) is used to validate the surface charge information of the catalysts (Fig. 7c). Specifically, the SPV signals of both the monometallic PW₁₂@Co and the bimetallic PW₁₂@CoNi are obviously higher than that of the PW₁₂@Cl⁻, where the SPV value of PW₁₂@Cl⁻ is almost close to zero. These results indicate that the surface charge characteristics of K₃PW₁₂O₄₀ are altered by the monometallic (Co) or bimetallic (CoNi) loading, which promotes the enhancement of the surface electric field, thereby facilitating the effective transfer of charges [43]. The increase in SPV signal of PW₁₂@CoNi is greater than that of PW₁₂@Co,

indicating that PW₁₂@CoNi has the best ability for transfer of charges among the three samples.

N₂ adsorption-desorption experiments were conducted to study the specific surface area of the dodecahedral yolk-shell structures of PW₁₂@Cl⁻, PW₁₂@Co and PW₁₂@CoNi (Fig. S23). All three photocatalysts exhibit type-IV N₂ adsorption isotherms, and the hysteresis loops do not display a distinct saturation adsorption plateau, indicating irregular pore structures [44]. Due to the presence of monometal (Co) and bimetal (Co and Ni) within the K₃PW₁₂O₄₀ framework, the BET specific surface area of PW₁₂@Co and PW₁₂@CoNi is smaller than that of PW₁₂@Cl⁻. Because of the uneven etching of PW₁₂@CoNi, its specific surface area is larger than that of uniformly etched PW₁₂@Co (Table S2) [45].

The physical and chemical adsorption properties of CO₂ over PW₁₂@Cl⁻, PW₁₂@Co and PW₁₂@CoNi are characterized by CO₂ adsorption isotherms (Fig. 7d). Under standard atmospheric pressure, the adsorption capacity of PW₁₂@Co and PW₁₂@CoNi for CO₂ is higher than that of PW₁₂@Cl⁻. This phenomenon could be attributed to the fact that PW₁₂@Cl⁻ only exhibits physical adsorption of CO₂. However, when loaded with Co and Ni, the adsorption behavior changes. In PW₁₂@Co and PW₁₂@CoNi, the presence of Co and Ni may enhance the chemical adsorption capability. This is because the Co and Ni active species can form more stable chemical bonds with CO₂ molecule. Therefore, the higher CO₂ adsorption capacity of PW₁₂@Co and PW₁₂@CoNi is due to their dual adsorption mechanisms [46]. The catalyst PW₁₂@CoNi with the highest carbon dioxide adsorption capacity shows the best CO₂ reduction activity.

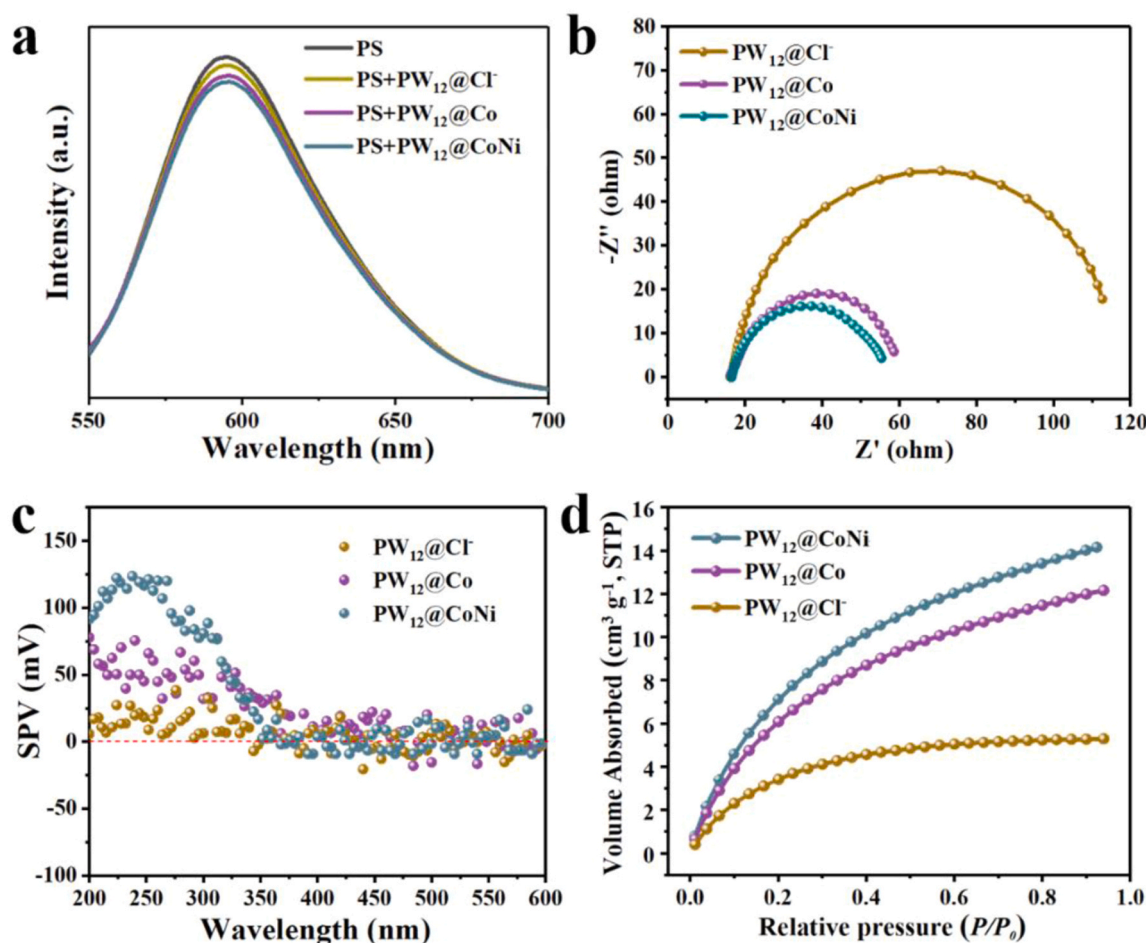


Fig. 7. PW₁₂ @Cl⁻, PW₁₂ @Co-6 h and PW₁₂ @Co-1/6Ni-6 h of (a) Steady-state PL spectra, (b) Electrochemical impedance spectra, (c) SPV spectra and (d) CO₂ adsorption curves.

Studying the reaction mechanism of CO₂RR is important for deep understanding and simulating the natural photosynthesis process (light reaction: $12\text{H}_2\text{O} \rightarrow 24\text{H}^+ + 24\text{e}^- + 6\text{O}_2$; dark reaction: $6\text{CO}_2 + 24\text{H}^+ + 24\text{e}^- \rightarrow (\text{CH}_2\text{O})_6 + 6\text{H}_2\text{O}$). Due to the involvement of multiple protons and electrons in the reactions, it is quite challenging to complete simulation the natural photosynthesis [47]. Therefore, by utilizing [Ru(bpy)₃]²⁺ to mimic the plant pigments for light absorption and providing electrons for CO₂RR, an artificial photosynthesis model reaction ($\text{CO}_2 + 2\text{H}^+ \rightarrow \text{CO} + \text{H}_2\text{O}$) could be established [48,49]. Consequently, PW₁₂ @Co and PW₁₂ @CoNi are employed to simulate the CO₂ reduction enzyme in the dark reaction of photosynthesis (Fig. 8a).

3.5. Transient absorption spectroscopy and mechanism investigation

To verify the feasibility of the artificial photosynthesis model, we investigated the catalytic behavior of PW₁₂ @CoNi catalyst in the photocatalytic CO₂ reduction process using transient absorption spectroscopy (TAS). Within the same time range, in the presence of PW₁₂ @CoNi and TEOA, PS could return to the ground state more effectively on a microsecond time scale. This indicates that PW₁₂ @CoNi can effectively maintain the recyclability of PS within the reaction system. In other words, PS can be re-excited and participate in the photocatalytic reaction, thereby enhancing the reaction efficiency and stability (Fig. 8b). Specifically, in the presence of only [Ru(bpy)₃]²⁺, under 460 nm light irradiation, the photosensitive [Ru(bpy)₃]²⁺ is excited to generate [Ru(bpy)₃]^{2+*}, which then spontaneously fades back to the ground state [Ru(bpy)₃]²⁺ via fluorescence quenching (Fig. 8c) [9]. However, in the

presence of both [Ru(bpy)₃]²⁺ and TEOA, the generated [Ru(bpy)₃]^{2+*} can be reduced to [Ru(bpy)₃]⁺ by TEOA and exhibits a longer lifetime. Without any catalyst, [Ru(bpy)₃]⁺ cannot spontaneously recover to [Ru(bpy)₃]²⁺ in the solution containing [Ru(bpy)₃]²⁺ and TEOA, and the signal at 450 nm in the transient absorption spectrum evolves into a long-life species (Fig. 8d) [50]. In the case of [Ru(bpy)₃]²⁺, TEOA and PW₁₂ @CoNi are present, the species of [Ru(bpy)₃]⁺ can be detected more easily than that of only PS. [Ru(bpy)₃]⁺ is then restored to the ground state [Ru(bpy)₃]²⁺ by giving electrons to PW₁₂ @CoNi (Fig. 8e). The mixture of [Ru(bpy)₃]²⁺, TEOA and PW₁₂ @CoNi achieves rapid bleaching recovery within a short time frame, indicating that the electron transfer from [Ru(bpy)₃]⁺ to PW₁₂ @CoNi is relatively fast [51].

3.6. In-situ diffuse reflectance infrared fourier transform spectroscopy investigation

For the purpose of examining the formation and transformation of intermediate products during the photocatalytic CO₂ reduction process, in-situ diffuse reflectance infrared Fourier transform spectroscopy (DRIFTS) tests was conducted over PW₁₂ @CoNi (Fig. 8f). Notably, the accumulation of different intermediate species is observed corresponds to the peaks in the infrared spectrum [52,53]. Moreover, the characteristic peaks at 1308 and 1520 cm⁻¹ are attributed to monodentate carbonate (m-CO₃²⁻) [54], while the characteristic peaks at 1414 and 1694 cm⁻¹ are attributed to bicarbonate (HCO₃⁻) [55–57]. All the aforementioned carbonate products are identified as intermediate products in the photocatalytic reduction of CO₂ to CO [58]. Importantly, we discover that the characteristic peaks at 1535 and 1670 cm⁻¹ belong

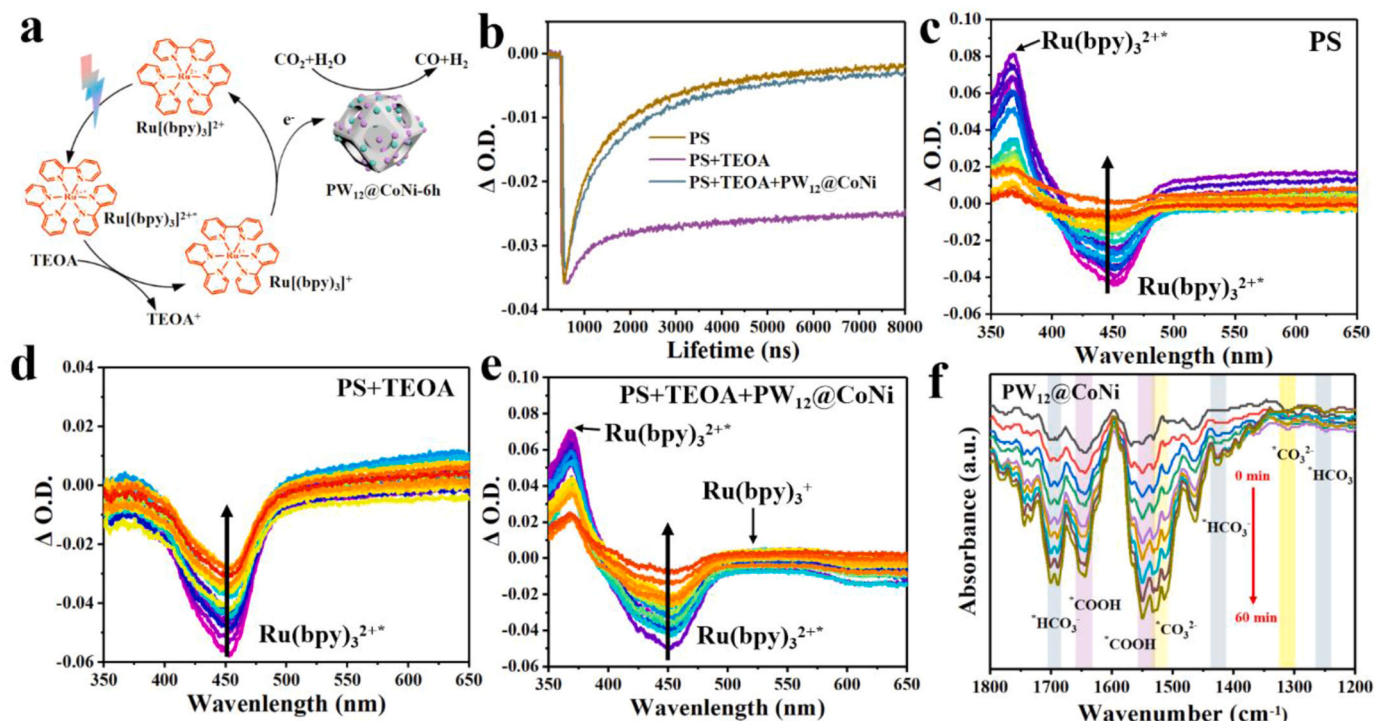


Fig. 8. (a) PW₁₂@CoNi in photosensitizer system CO₂ reduction mechanism diagram, (b) Recovery kinetics of transient bleaching recovery for PS monitored with PW₁₂@CoNi, and transient absorption spectra of (c) PS, (d) PS+TEOA, (e) PS+TEOA+PW₁₂@CoNi and (f) in situ DRIFTS of PW₁₂@CoNi for CO₂ reduction under visible light irradiation.

to *COOH which is a significant intermediate of CO production, elucidating the crucial conversion process in photocatalytic CO₂ reduction [59,60]. As the irradiation time extends, the absorption peaks of all intermediates progressively enhance, signifying the ongoing photocatalytic reaction.

3.7. Density functional theory calculations

The Gibbs free energy of H₂ and CO evolution in PW₁₂@Co and PW₁₂@CoNi are analyzed by DFT calculations, which are supplementarily supported by calculations of the work function and d-band center. The calculation of the Gibbs free energy for hydrogen evolution reveals

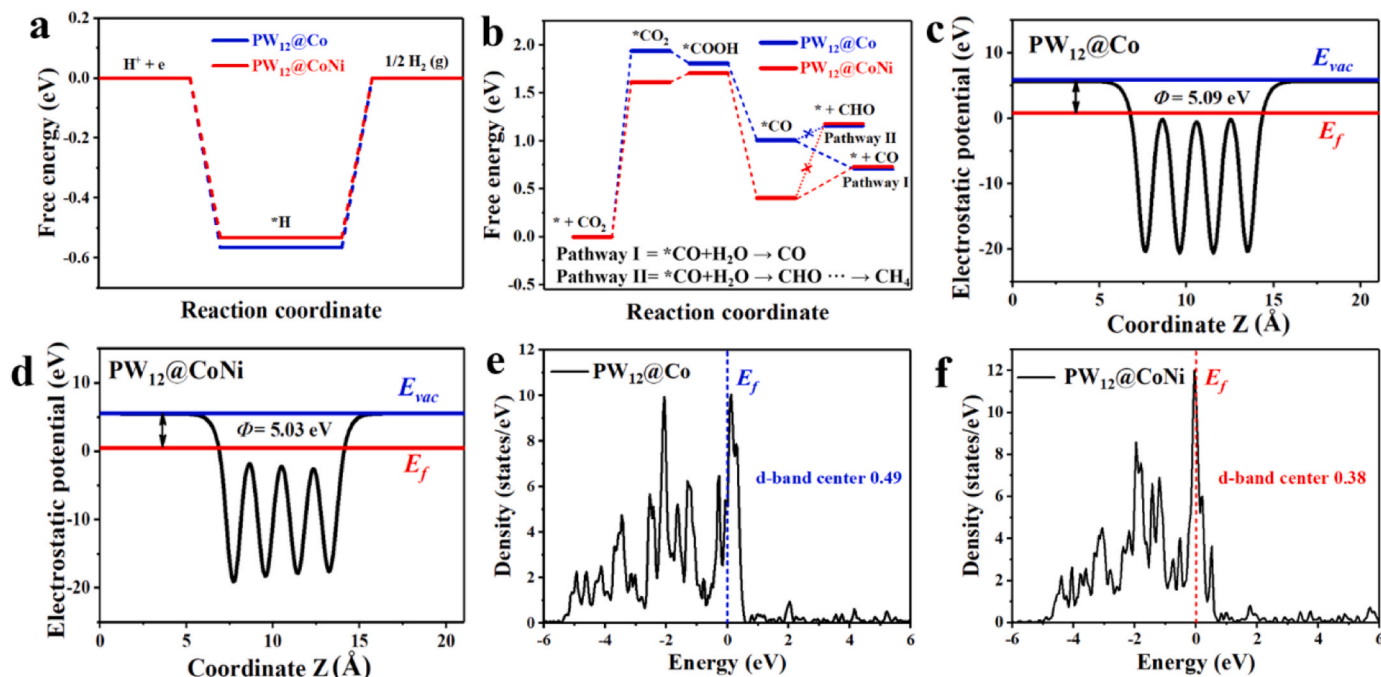


Fig. 9. PW₁₂@Co and PW₁₂@CoNi of (a, b) work function calculations, (c) Gibbs free energy calculations for H₂ evolution, (d, e) d-band center calculations and (f) basic steps and Gibbs free energy calculations of the CO₂RR.

that the adsorption of H₂ on different metal sites over PW₁₂@Co (111) and PW₁₂@CoNi (111) surfaces has negative values, indicating exothermic adsorption of hydrogen (Fig. 9a) [9]. Moreover, the rate-determining step for both PW₁₂@Co and PW₁₂@CoNi is hydrogen desorption, with PW₁₂@CoNi exhibiting a lower barrier (0.53 eV) compared to PW₁₂@Co (0.57 eV). Therefore, due to its stronger ability to form H* intermediates and lower hydrogen desorption barrier, PW₁₂@CoNi has an advantage in photocatalytic hydrogen production [50]. These computational results are consistent with the observed trends in hydrogen evolution activity.

Furthermore, the calculation of the Gibbs free energy for the CO₂ reduction reaction reveals that CO₂ undergoes adsorption, *COOH intermediate formation and CO desorption processes [61,62]. The adsorption of CO₂ on mono- and bimetallic sites over PW₁₂@Co and PW₁₂@CoNi is found to be the rate-determining step for CO₂ reduction, with ΔG values of 1.94 and 1.61 eV, respectively. Therefore, PW₁₂@CoNi exhibits a lower CO₂ adsorption energy barrier, which is consistent with previous CO₂ adsorption test results, indicating its ability to efficiently adsorb CO₂ in the photocatalytic CO₂RR process. Furthermore, for PW₁₂@Co, the formation of the *CHO intermediate in the CH₄ production process is an endothermic process, while CO desorption is an exothermic process, making it more thermodynamically favorable. For PW₁₂@CoNi, the energy barrier for *CHO formation is higher than the CO desorption barrier, suggesting that CO desorption is thermodynamically favorable. Therefore, the gas product over both PW₁₂@Co and PW₁₂@CoNi contains CO and H₂ (Fig. 9b) [63].

The energy required for Fermi-level electrons to escape from a potential well at depth X is defined as the work function (WF). Indeed, the work function represents the ability of a material to attract electrons [64–67]. PW₁₂@CoNi has a lower work function (φ = 5.03) compared to PW₁₂@Co (φ = 5.09) (Fig. 9c–d). A smaller work function means a relatively higher Fermi level, indicating that the material is more likely to accept electrons from external sources. Therefore, PW₁₂@CoNi can accept more electrons from PS, which is consistent with lower activation barriers for HER and CO₂RR over PW₁₂@CoNi. This affords higher activity of PW₁₂@CoNi in HER and CO₂RR reactions. According to the d-band center theory, the d-band center value of a catalyst's transition metal atoms is correlated with their affinity for binding with H [68–70]. Calculations indicate that the d-band center value of PW₁₂@CoNi (0.38) is lower than that of PW₁₂@Co (0.49), which suggests that PW₁₂@CoNi has a weaker combination ability for H₂ corresponding to its lower hydrogen desorption energy barrier (Fig. 9e–f). Consequently, based on DFT calculations, it is concluded that PW₁₂@CoNi exhibits a stronger ability to adsorb CO₂, lower hydrogen desorption energy and the ability to accept more electrons from PS in comparison to PW₁₂@Co.

4. Conclusion

In this work, we employed a simple strategy of adjusting dodecahedral K₃PW₁₂O₄₀ polyoxometalate morphology evolution via ion exchange, hydrothermal etching and annealing. A series of catalysts with yolk-shell and hollow structure were prepared and used for the CO₂RR. Among the mono- or bimetallic species (Co or CoNi) supported on yolk-shell structure K₃PW₁₂O₄₀ catalysts, PW₁₂@Co-1/6Ni behaves the best CO production rate and selectivity. The difference in activity between PW₁₂@Co and PW₁₂@CoNi originates from the structural transformation of the dodecahedra during hydrothermal etching and the effect of loading mono- and bimetallic species on K₃PW₁₂O₄₀. The electron transfer rate difference between PW₁₂@Co and PW₁₂@CoNi is confirmed by photo/electrochemical characterization. Furthermore, DFT calculations and CO₂ adsorption experiments of PW₁₂@Co and PW₁₂@CoNi reveal differences in selectivity for CO. Overall, this work provides an effective method for improving CO₂RR by utilizing polyoxometalates with morphology evolution as supports and incorporating Co or CoNi as catalytic active sites, which offers valuable insights for the design of efficient CO₂ reduction photocatalysts.

CRedit authorship contribution statement

Li Bonan: Conceptualization, Data curation, Investigation, Visualization, Writing – original draft, Writing – review & editing. **Chen Mengxue:** Data curation, Formal analysis, Investigation, Visualization, Writing – review & editing. **Hu Qiyu:** Investigation, Visualization, Writing – review & editing. **Zhu Jiayu:** Software, Supervision, Writing – review & editing. **Yang Xu:** Investigation, Visualization. **Li Zhexu:** Validation, Visualization. **Hu Chunlian:** Validation, Visualization. **Li Yuanyuan:** Resources, Software. **Ni Ping:** Funding acquisition. **Ding Yong:** Conceptualization, Formal analysis, Funding acquisition, Supervision, Writing – original draft, Writing – review & editing.

Declaration of Competing Interest

The authors declare that they have no known competing financial interests or personal relationships that could have appeared to influence the work reported in this paper.

Data availability

Data will be made available on request.

Acknowledgements

This work was financially supported by the National Natural Science Foundation of China (22075119 and 22209017), the Natural Science Foundation of Gansu Province (21JR7RA440) and State Key Laboratory of Chemical Resource Engineering Beijing University of Chemical Technology (CRE-2023-01-01).

Appendix A. Supporting information

Supplementary data associated with this article can be found in the online version at doi:10.1016/j.apcatb.2024.123733.

References

- [1] S. Chu, A. Majumdar, Opportunities and challenges for a sustainable energy future, *Nature* 488 (2012) 294–303.
- [2] A. Dolbecq, E. Dumas, C.R. Mayer, P. Mialane, Hybrid organic-inorganic polyoxometalate compounds: from structural diversity to applications, *Chem. Rev.* 110 (2010) 6009–6048.
- [3] J.M. Lehn, R. Ziessel, Photochemical generation of carbon monoxide and hydrogen by reduction of carbon dioxide and water under visible light irradiation, *Proc. Natl. Acad. Sci. U. S. A.* 79 (1982) 701–704.
- [4] M. Nyman, P.C. Burns, Comprehensive comparison of transition-metal and actinyl polyoxometalates, *Chem. Soc. Rev.* 41 (2012) 7354–7367.
- [5] M. Nyman, Polyoxoniobate Chemistry, in the 21st century, *Dalton Trans.* 40 (2011) 8049–8058.
- [6] H. Kumagai, Y. Tamaki, O. Ishitani, Photocatalytic systems for CO₂ reduction: metal-complex photocatalysts and their hybrids with photofunctional solid materials, *Acc. Chem. Res.* 55 (2022) 978–990.
- [7] E. Pugliese, P. Gotico, I. Wehrung, B. Boitrel, A. Quaranta, M.H. Ha-Thi, T. Pino, M. Sircoglou, W. Leibl, Z. Halime, A. Aukauloo, Dissection of light-induced charge accumulation at a highly active iron porphyrin: insights in the photocatalytic CO₂ reduction, *Angew. Chem. Int. Ed.* 61 (2022), 202202924.
- [8] Y.J. Dong, Q.Y. Hu, B.N. Li, X.H. Li, M.X. Chen, M.Y. Zhang, Y. Feng, Y. Ding, Aminated silicon dioxide enriching iron-containing polyoxometalate catalyst confined in Cds for efficient H₂ evolution, *Appl. Catal. B-Environ.* 304 (2022) 120998.
- [9] X.Y. Meng, J.Y. Yang, C.C. Zhang, Y.F. Fu, K. Li, M.H. Sun, X.G. Wang, C.Z. Dong, B.C. Ma, Y. Ding, Light-driven CO₂ reduction over prussian blue analogues as heterogeneous catalysts, *ACS Catal.* 12 (2022) 89–100.
- [10] Y. Feng, C. Wang, P. Cui, C. Li, B. Zhang, L. Gan, S. Zhang, X. Zhang, X. Zhou, Z. Sun, K. Wang, Y. Duan, H. Li, K. Zhou, H. Huang, A. Li, C. Zhuang, L. Wang, Z. Zhang, X. Han, Ultrahigh photocatalytic CO₂ reduction efficiency and selectivity manipulation by single-tungsten-atom oxide at the atomic step of TiO₂, *Adv. Mater.* 34 (2022) 2109074.
- [11] A. Misra, K. Kozma, C. Streb, M. Nyman, Beyond charge balance: counter-cations in polyoxometalate chemistry, *Angew. Chem. Int. Ed.* 59 (2020) 596–612.
- [12] M. Anjass, G.A. Lowe, C. Streb, Molecular vanadium oxides for energy conversion and energy storage: current trends and emerging opportunities, *Angew. Chem. Int. Ed.* 60 (2021) 7522–7532.

- [13] M. Lu, M. Zhang, J. Liu, T.Y. Yu, J.N. Chang, L.J. Shang, S.L. Li, Y.Q. Lan, Confining and highly dispersing single polyoxometalate clusters in covalent organic frameworks by covalent linkages for CO₂, *Photo J. Am. Chem. Soc.* 144 (2022) 1861–1871.
- [14] J. Gu, W. Chen, G.G. Shan, G. Li, C. Sun, X.L. Wang, Z. Su, The roles of polyoxometalates in photocatalytic reduction of carbon dioxide. *Mater. Today Energy* 21 (2021) 100760.
- [15] G. Izzet, B. Abecassis, D. Brouri, M. Piot, B. Matt, S.A. Serapian, C. Bo, A. Proust, Hierarchical self-assembly of polyoxometalate-based hybrids driven by metal coordination and electrostatic interactions: from discrete supramolecular species to dense monodisperse nanoparticles, *J. Am. Chem. Soc.* 138 (2016) 5093.
- [16] M.X. Chen, K. Umer, B.N. Li, Z.X. Li, K.M. Li, W.J. Sun, Y. Ding, Metalloporphyrin based MOF-545 coupled with solid solution Zn₃Cd_{1-x}S for efficient photocatalytic hydrogen production, *J. Colloid Interf. Sci.* 653 (2024) 380–389.
- [17] B. Chakraborty, G. Gan-Or, Y. Duan, M. Raula, I.A. Weinstock, Visible-light-driven water oxidation with a polyoxometalate-complexed hematite core of 275 iron atoms, *Angew. Chem. Int. Ed.* 58 (2019) 6584–6589.
- [18] X.Q. Du, J.L. Zhao, J.Q. Mi, Y. Ding, P.P. Zhou, B.C. Ma, J.W. Zhao, J. Song, Efficient photocatalytic H₂ evolution catalyzed by an unprecedented robust molecular semiconductor {Fe1} nanocluster without cocatalysts at neutral conditions, *Nano Energy* 16 (2015) 247–255.
- [19] H.J. Lv, W.W. Guo, K.F. Wu, Z.Y. Chen, J. Bacsa, D.G. Musaev, Y.R.V. Geletii, S. M. Lauinger, T.Q. Lian, C.L. Hill, A noble-metal-free, tetra-nickel polyoxotungstate catalyst for efficient photocatalytic hydrogen evolution, *J. Am. Chem. Soc.* 136 (2014) 14015–14018.
- [20] F.Y. Song, Y. Ding, B.C. Ma, C.M. Wang, Q. Wang, X.Q. Du, S. Fu, J. Song, K₇[Co^{III}Co^{II}][H₂O]W₁₁O₃₉: a molecular mixed-valence Keggin polyoxometalate catalyst of high stability and efficiency for visible light-driven water oxidation, *Energy Environ. Sci.* 6 (2013) 1170–1184.
- [21] Q.S. Yin, J.M. Tan, C. Besson, Y.V. Geletii, D.G. Musaev, A.E. Kuznetsov, Z. Luo, K. I. Hardcastle, C.L. Hill, A fast soluble carbon-free molecular water oxidation catalyst based on abundant metals, *Science* 328 (2010) 342–345.
- [22] L. Yang, J. Zhao, J.W. Zhao, J.Y. Niu, Syntheses, crystal structures, and magnetic properties of the banana-shaped tungstophosphates: [M₆(H₂O)₂[PW₉O₃₄]₂[PW₆O₂₆]]¹⁷⁻ [M^{II}=Ni^{II}, Co^{II}], *J. Coord. Chem.* 65 (2012) 3363–3371.
- [23] J. Wei, Y.Y. Feng, P.P. Zhou, Y. Liu, J.Y. Xu, R. Xiang, Y. Ding, C.C. Zhao, L.Y. Fan, C.W. Hu, A bioinspired molecular polyoxometalate catalyst with two cobalt(III) oxide cores for photocatalytic water oxidation, *ChemSusChem* 8 (2015) 2630–2634.
- [24] X.B. Han, Y.G. Li, Z.M. Zhang, H.Q. Tan, Y. Lu, E.B. Wang, Polyoxometalate-based, Nickel Clust. Visible Light-driven Water Oxid. *Catal. J. Am. Chem. Soc.* 137 (2015) 5486–5493.
- [25] H.J. Yu, E. Haviv, R. Neumann, visible-light photochemical reduction of CO₂ to CO coupled to hydrocarbon dehydrogenation, *Angew. Chem. Int. Ed.* 59 (2020) 6219–6223.
- [26] Z. Wang, L. Wang, Progress in designing effective photoelectrodes for solar water splitting, *Chin. J. Catal.* 39 (2018) 369–378.
- [27] M. Xiao, Z. Wang, M. Lyu, B. Luo, S. Wang, G. Liu, H.M. Cheng, L. Wang, Hollow nanostructures for photocatalysis: advantages and challenges, *Adv. Mater.* 31 (2019) 1801369.
- [28] X. Li, J. Liu, A.F. Masters, V.K. Pareek, T. Maschmeyer, Hollow micro/nanomaterials as nanoreactors for photocatalysis, *APL Mater.* 1 (2013) 041101.
- [29] F. Le Formal, S.R. Pendlebury, M. Cornuz, S.D. Tilley, M. Grätzel, J.R. Durrant, Back electron-hole recombination in hematite photoanodes for water splitting, *J. Am. Chem. Soc.* 136 (2014) 2564–2574.
- [30] X.W. Lou, L.A. Archer, Z. Yang, Hollow micro-/nanostructures: synthesis and applications, *Adv. Mater.* 20 (2008) 3987–4019.
- [31] W.J. Luo, J. Hu, H.L. Diao, B. Schwarz, C. Streb, Y.F. Song, Robust polyoxometalate/nickel foam composite electrodes for sustained electrochemical oxygen evolution at high pH, *Angew. Chem. Int. Ed.* 56 (2017) 4941–4944.
- [32] Q.L. Kang, D.W. Lai, M.F. Su, B.R. Xiong, W.Y. Tang, Q.Y. Lu, F. Gao, Tailored dodecahedral polyoxometalates nanoframes with in situ encapsulated Co, N, C for oxygen evolution reaction, *Chem. Eng. J.* 430 (2022) 133116.
- [33] X.L. Chen, P. Huang, X. Zhu, S.X. Zhuang, H.C. Zhu, J.J. Fu, A.S. Nissimogoudar, W. Li, X.W. Zhang, L. Zhou, Y. Wang, Z.Y. Lv, Y. Zhou, S.T. Han, Keggin-type polyoxometalate cluster as an active component for redox-based nonvolatile memory, *Nanoscale Horiz.* 4 (2019) 697–704.
- [34] Q.Y. Li, L. Zhang, Y.X. Xu, Q. Li, H.G. Xue, H. Pang, Smart yolk/shell ZIF-67@POM hybrids as efficient electrocatalysts for the oxygen evolution reaction. *ACS Sustain. Chem. Eng.* 7 (2019) 5027–5033.
- [35] S. Zhang, S.R. Zhao, S.J. Huang, B. Hu, M.H. Wang, Z.H. Zhang, L.H. He, M. Du, Photocatalytic degradation of oxytetracycline under visible light by nanohybrids of CoFe alloy nanoparticles and nitrogen-/sulfur-codoped mesoporous carbon, *Chem. Eng. J.* 420 (2021) 130516.
- [36] X.H. Lin, S.B. Wang, W.G. Tu, H.J. Wang, Y.D. Hou, W.X. Dai, R. Xu, Magnetic Hollow spheres assembled from graphene-encapsulated nickel nanoparticles for efficient photocatalytic CO₂ reduction, *ACS Appl. Energy Mater.* 2 (2019) 7670–7678.
- [37] Y.B. Guo, S. Yao, Y.Y. Xue, X. Hu, H.J. Cui, Z. Zhou, Nickel single-atom catalysts intrinsically promoted by fast pyrolysis for selective electroreduction of CO₂ into CO, *Appl. Catal. B-Environ.* 304 (2022) 120997.
- [38] Y.X. Wang, M.J. Wu, J. Li, H.T. Huang, J.L. Qiao, In situ growth of CoP nanoparticles anchored on (N, P) co-doped porous carbon engineered by MOFs as advanced bifunctional oxygen catalyst for rechargeable Zn-air battery, *J. Mater. Chem. A* 8 (2020) 19043–19049.
- [39] P.F. Wang, Y. Li, S.H. Tian, J.C. Wang, F.L. Qiu, Y.R. Zhu, T.F. Yi, P. He, Freestanding and consecutive intermixed N-doped hard Carbon@Soft carbon fiber architectures as Ultrastable anodes for high-performance Li-ion batteries, *Energy Fuels* (2023) 15170–15178.
- [40] J. Wu, M. Jin, Y. Li, J.F. Zhao, T.T. Wang, Y.H. Xie, L.Q. Liu, C.B. Wang, F.W. Li, Earth-abundant Co nanoparticles encapsulated in N-doped hollow carbon sphere for highly selective hydrodeoxygenation of biomass-derived vanillin, *Chem. Eng. J.* 463 (2023) 142472.
- [41] J. Zhou, W. Chen, C. Sun, L. Han, C. Qin, M. Chen, X.L. Wang, E.B. Wang, Z.M. Su, Oxidative polyoxometalates modified graphitic carbon nitride for visible-light CO₂ reduction, *ACS Appl. Mater. Interfaces* 9 (2017) 11689–11695.
- [42] Y.J. Wang, G.L. Zhuang, J.W. Zhang, F. Luo, X. Cheng, F.L. Sun, S.S. Fu, T.B. Lu, Z. M. Zhang, Co-dissolved isostructural polyoxovanadates to construct single-atom-site catalysts for efficient CO₂ photoreduction, *Angew. Chem. Int. Ed.* 62 (2022) e202216592.
- [43] J. Zhu, F.T. Fan, R.T. Chen, H.Y. An, Z.C. Feng, C. Li, Direct imaging of highly anisotropic photogenerated charge separations on different facets of a single BiVO₄ photocatalyst, *Angew. Chem. Int. Ed.* 54 (2015) 9111–9114.
- [44] Z. Zhang, Y.W. Liu, H.R. Tian, X.J. Ma, Q. Yue, Z.X. Sun, Y. Lu, S.X. Liu, Hierarchically ordered macro-microporous polyoxometalate-based metal-organic framework single crystals, *ACS Nano* 15 (2021) 16581–16588.
- [45] L. Wang, J.W. Wan, Y.S. Zhao, N.L. Yang, D. Wang, Hollow multi-shelled structures of Co₃O₄ dodecahedron with unique crystal orientation for enhanced photocatalytic CO₂ reduction, *J. Am. Chem. Soc.* 141 (2019) 2238–2241.
- [46] X.H. Lin, S.B. Wang, W.G. Tu, H.J. Wang, Y.D. Hou, W.X. Dai, R. Xu, Magnetic hollow spheres assembled from graphene-encapsulated nickel nanoparticles for efficient photocatalytic CO₂ reduction, *ACS Appl. Energy Mater.* 2 (2019) 7670–7678.
- [47] J. Lin, X. Liang, X. Cao, N. Wei, Y. Ding, An octanuclear Cu(II) cluster with a bio-inspired Cu₄O₄ cubic fragment for efficient photocatalytic water oxidation, *Chem. Commun.* 54 (2018) 12515–12518.
- [48] Z.L. Wang, S.A. Monny, L.Z. Wang, Hollow structure for photocatalytic CO₂ reduction, *ChemNanoMat* 6 (2020) 881–888.
- [49] C.Q. Chang, X. Meng, W. Ruan, Y. Feng, R. Li, J. Zhu, Y. Ding, H. Lv, W. Wang, G. Chen, X. Fang, Metal-organic cages with {SiW₉Ni₄} polyoxotungstate nodes, *Angew. Chem. Int. Ed.* 61 (2022) e202117637.
- [50] X.Y. Meng, R. Li, J.Y. Yang, S.M. Xu, C.C. Zhang, K.J. You, B.C. Ma, H.X. Guan, Y. Ding, Hexanuclear ring cobalt complex for photochemical CO₂ to CO conversion, *Chinese, J. Catal.* 43 (2022) 2414–2424.
- [51] Q.Y. Hu, S.S. Chen, T. Wagberg, H.S. Zhou, S.J. Li, Y.D. Li, Y.L. Tan, W.Q. Hu, Y. Ding, X.B. Han, Developing insoluble polyoxometalate clusters to bridge homogeneous and heterogeneous water oxidation photocatalysis, *Angew. Chem. Int. Ed.* 62 (2023) e202303290.
- [52] J. Wu, X.D. Li, W. Shi, P.Q. Ling, Y.F. Sun, X.C. Jiao, S. Gao, L. Liang, J.Q. Xu, W. S. Yan, C.M. Wang, Y. Xie, Efficient visible-light-driven CO₂ reduction mediated by defect-engineered biobir atomic layers, *Angew. Chem. Int. Ed.* 57 (2018) 8719–8723.
- [53] N.X. Li, B.B. Wang, Y.Y. Si, F. Xue, J.C. Zhou, Y.J. Lu, M.C. Liu, Toward high-value hydrocarbon generation by photocatalytic reduction of CO₂ in water vapor, *ACS Catal.* 9 (2019) 5590–5602.
- [54] N.T. Taylor, F.H. Davies, S.G. Davies, C.J. Price, S.P. Hepplestone, The fundamental mechanism behind colossal permittivity in oxides, *Adv. Mater.* 31 (2019) 1904746.
- [55] S.Y. Zhu, W.R. Liao, M.Y. Zhang, S.J. Liang, Design of spatially separated Au and CoO dual cocatalysts on hollow TiO₂ for enhanced photocatalytic activity towards the reduction of CO₂ to CH₄, *Chem. Eng. J.* 361 (2019) 461–469.
- [56] X.D. Li, Y.F. Sun, J.Q. Xu, Y.J. Shao, J. Wu, X.L. Xu, Y. Pan, H.X. Ju, J.F. Zhu, Y. Xie, selective visible-light-driven photocatalytic CO₂ reduction to CH₄ mediated by atomically thin CuInS₂ layers, *Nat. Energy* 4 (2019) 690–699.
- [57] Y.Z.Z. Yu, K. Yang, C.L. Yu, K.Q. Lu, W.Y. Huang, L. Xu, L.X. Zou, S.B. Wang, Z. Chen, J. Hu, Y. Hou, Y.F. Zhu, Steering unit cell dipole and internal electric field by highly dispersed er atoms embedded into nio for efficient CO₂ photoreduction, *Adv. Funct. Mater.* 32 (2022) 2111999.
- [58] Y. Yang, H.Y. Zhang, Y. Wang, L.H. Shao, L. Fang, H. Dong, M. Lu, L.Z. Dong, Y. Q. Lan, F.M. Zhang, Integrating enrichment, reduction, and oxidation sites in one system for artificial photosynthetic diluted CO₂ reduction, *Adv. Mater.* 35 (2023) 2304170.
- [59] S. Karmakar, S. Barman, F.A. Rahimi, T.K. Maji, Covalent grafting of molecular Photosensitizer and catalyst on MOF-808: effect of pore confinement toward visible light-driven CO₂ reduction in water, *Energy Environ. Sci.* 14 (2021) 2429–2440.
- [60] M. Wang, M. Shen, X.X. Jin, J.J. Tian, M.L. Li, Y.J. Zhou, L.X. Zhang, Y.S. Li, J. L. Shi, Oxygen vacancy generation and stabilization in CeO_{2-x} by Cu introduction with improved CO₂ photocatalytic reduction activity, *ACS Catal.* 9 (2019) 4573–4581.
- [61] J.H. Ding, X.Y. Guan, J. Lv, X.H. Chen, Y. Zhang, H. Li, D.L. Zhang, S.L. Qiu, H. L. Jiang, Q.R. Fang, Three-dimensional covalent organic frameworks with ultra-large pores for highly efficient photocatalysis, *J. Am. Chem. Soc.* 145 (2023) 3248–3254.
- [62] Y.X. Liu, J. Wu, F. Wang, Dibenzothiophene-S, S-dioxide-containing conjugated polymer with hydrogen evolution rate up to 147 mmol/g h⁻¹, *Appl. Catal. B-Environ.* 307 (2022) 121144.
- [63] M. Zhou, Z.Q. Wang, A.H. Mei, Z.F. Yang, W. Chen, S.Y. Ou, S.Y. Wang, K.Q. Chen, P. Reiss, K. Qi, J.Y. Ma, Y.L. Liu, Photocatalytic CO₂ reduction using La-Ni bimetallic sites within a covalent organic framework, *Nat. Commun.* 14 (2023) 2473.

- [64] B.C. Yang, B.S. Wan, Q.H. Zhou, Y. Wang, W.T. Hu, W.M. Lv, Q. Chen, Z.M. Zeng, F.S. Wen, J.Y. Xiang, S.J. Yuan, J.L. Wang, B.S. Zhang, W.H. Wang, J.Y. Zhang, B. Xu, Z.S. Zhao, Y.J. Tian, Z.Y. Liu, Te-doped Black Phosphorus Field-Eff. Transistors Adv. Mater. 28 (2016) 9408–9415.
- [65] X.Y. Cai, Y.Z. Chen, B. Sun, J. Chen, H.Y. Wang, Y.X. Ni, L. Tao, H. Wang, S.H. Zhu, X.M. Li, Y.C. Wang, J. Lv, X.L. Feng, S.A.T. Redfern, Z.F. Chen, Two-dimensional blue-AsP monolayers with tunable direct band gap and ultrahigh carrier mobility show promising high-performance photovoltaic properties, Nanoscale 11 (2019) 8260–8269.
- [66] C.H. Hu, Y.J. Wang, J.M. Chen, H.F. Wang, K. Shen, K.W. Tang, L.Y. Chen, Y.W. Li, Main-Group metal single-atomic regulators in dual-metal catalysts for enhanced electrochemical CO₂ reduction, Small 18 (2022) 2201391.
- [67] R.J. Zeng, K.K. Lian, B. Su, L.L. Lu, J.W. Lin, D.P. Tang, S. Lin, X.C. Wang, Versatile synthesis of hollow metal sulfides via reverse cation exchange reactions for photocatalytic CO₂ reduction, Angew. Chem. Int. Ed. 60 (2021) 25055.
- [68] J.K. Nørskov, F.A. Pedersen, F. Studt, T. Bligaard, Density functional theory in surface chemistry and catalysis, Proc. Natl. Acad. Sci. U. S. A. 108 (2011) 937–943.
- [69] Z.J. Zhao, S. Liu, S. Zha, D. Cheng, F. Studt, G. Henkelman, J. Gong, Theory-guided design of catalytic materials using scaling relationships and reactivity descriptors, Nat. Rev. Mater. 4 (2019) 792–804.
- [70] J.K. Nørskov, T. Bligaard, J. Rossmeisl, C.H. Christensen, Towards the computational design of solid catalysts, Nat. Chem. 1 (2009) 37–46.